

Reliability of Marine Structures Program

SPAR FLOATING PLATFORM: NUMERICAL ANALYSIS AND COMPARISON WITH DATA

Alok K. Jha

Supervised by
Steven R. Winterstein

Civil Engineering Department, Stanford University

DISTRIBUTION STATEMENT A
Approved for Public Release
Distribution Unlimited

June 1997

Report No. RMS-25



Department of CIVIL ENGINEERING
STANFORD UNIVERSITY

20011123 059

**SPAR FLOATING PLATFORM:
NUMERICAL ANALYSIS AND
COMPARISON WITH DATA**

Alok K. Jha

Supervised by
Steven R. Winterstein

Civil Engineering Department, Stanford University

June 1997
Report No. RMS-25

Acknowledgements

This study is part of the doctoral work of the author and has been supported by the Offshore Technology Research Center (OTRC). Additional funding has been provided by the Reliability of Marine Structures (RMS) program at Stanford University. The author thanks OTRC for providing the measured wave tank data on the spar platform tests.

Abstract

Second-order nonlinear models have been increasingly used in recent years to model nonlinear processes in offshore engineering. We apply such models to study the global responses of a spar floating platform. Traditional linear models of wave loads on offshore structures tend to be inaccurate in the response predictions. Second-order nonlinear models although computationally more expensive provide an opportunity to better predict these loads.

Recent tests conducted on a spar floating platform offer wave tank data for extreme conditions in both the Gulf of Mexico and the North Sea. We model the tested spar floating platform as a linear rigid-body with 6 degrees of freedom. The incident wave loads are modeled as a second-order phenomenon. Of interest is the global response of the spar, which here is the total horizontal displacement near the spar deck. Although the apparent transient response and the few measured response cycles pose difficulties in calibrating the model, we find the model to offer reasonable predictions when compared to the measured results in wave tanks.

Contents

Acknowledgements	iii
Abstract	v
1 Introduction	1
2 Spar Model for Slow-drift Response	3
2.1 Experimental Data	3
2.2 Structural Model	11
2.3 Hydrodynamic Model Forms	15
2.4 Input Wave Histories for Models	18
2.5 Calibrated Damping Values	19
2.6 Estimation of Initial Conditions	22
3 Results	25
3.1 Wave-frequency (first-order) Response	25
3.2 Surge (DOF1) and Pitch (DOF5) Component Responses	29
3.3 Total Predicted Horizontal Displacement	41
4 Conclusion and Future Work	47
4.1 Conclusion	47
4.2 Future Work	48
Bibliography	50

A First-order Wave Identification	55
B QTF-surface Spline Interpolation	61
B.1 Introduction	61
B.2 Interpolation Options	62
B.3 Verification Studies of FITQTF Interpolation	64
C Paper to be Presented at BOSS97	69

List of Tables

2.1	Details of the spar configuration (in prototype scale)	4
2.2	Reference wave summary statistics for the OTRC wave tank tests used for slow-drift response analysis of the spar	7
2.3	Statistical moments of the measured horizontal displacements for the seastates. Note that the maximum and minimum values contain μ . .	10
2.4	Statistical moments of the filtered components (with zero mean) of measured horizontal displacements	10
2.5	Nomenclature for the four proposed model forms	18
2.6	Calibrated damping ratios (%), ξ , for the models in surge (DOF1) and pitch (DOF5) components	21
2.7	Estimated initial conditions in surge and pitch DOFs for the three seastates	23
B.1	Description of error messages from FITQTF	63

List of Figures

2.1	Elevation view of Spar platform	4
2.2	Degrees of freedom for spar	5
2.3	Spectrum of measured surge displacements at 54.8m elevation above MWL for GOM1 seastate	9
2.4	Total measured horizontal displacement and its filtered surge, pitch and wave-frequency components for GOM1 seastate	12
2.5	Reference (observed) wave vs. underlying first- and second-order waves	20
3.1	Comparison of the first-order (wave-frequency) response statistics: Stan- dard deviation σ_1 (top left), maximum normalized by the standard deviation (top right) and absolute maximum displacements (bottom)	27
3.2	Comparison of predicted first-order response time histories to mea- surements across the three tests. For clarity we show only 500-second portions of each test, selected to include the absolute maximum observed response.	28
3.3	Comparison of statistical moments for surge and pitch components in the three seastates: Predictions from the four models vs. measure- ments. The moments include total mean, and standard deviations in surge and pitch frequency components (see titles in the figure).	34
3.4	Comparison of statistical moments for surge and pitch components in the three seastates: Predictions from the four models vs. measure- ments. The moments include maximum normalized by the standard deviation and the absolute (unnormalized) maximum displacements in each of surge and pitch frequency components (see titles in the figure).	35

3.5	Comparison of (zero-mean) response time histories in DOF1: prediction vs. measurement	36
3.6	Zero-mean pitch (DOF5) time histories for GOM1: prediction vs. measurement	37
3.7	Zero-mean pitch (DOF5) time histories for GOM2: prediction vs. measurement	38
3.8	Zero-mean pitch (DOF5) time histories for NS: prediction vs. measurement	39
3.9	Second-order (=surge+pitch components) predicted and measured response to indicate preservation of net input initial conditions found from observed histories	40
3.10	Comparison of standard deviation and maximum of combined response: prediction vs. measurement	43
3.11	Combined (total) surge response time history for GOM1: prediction vs. measurement	44
3.12	Combined (total) surge response time history for GOM2: prediction vs. measurement	45
3.13	Combined (total) surge response time history for NS: prediction vs. measurement	46
B.1	Frequency grid points of the sparse and the finely meshed QTF values from SWIM	64
B.2	Direct statistics mean for interpolated QTFs from sparse QTF vs. exact mean from finely meshed QTF (from diffraction analysis)	67
B.3	Direct statistics standard deviation for interpolated QTFs from sparse QTF vs. exact mean from finely meshed QTF	67
B.4	1-hour predicted mean for interpolated QTFs from sparse QTF vs. exact mean from finely meshed QTF	68
B.5	1-hour predicted standard deviation for interpolated QTFs from sparse QTF vs. exact mean from finely meshed QTF	68

Chapter 1

Introduction

In this study, we will investigate the global response behavior of a large-volume floating structure (here, a spar platform) and compare model predictions to measurements in wave tank tests on this structure. Given good agreement to data, the model can then be used as a tool in designing various structural components of the spar.

Large-volume floating structures are being increasingly used for deep-water drilling and production of oil and natural gas. Examples of such structures include tension-leg platforms (TLP), semi-submersibles and spar floating platforms. For a TLP the deck is placed on a hull made up of three to five columns, with the columns extending into the water and connected to each other by pontoons. The floating hull is held down to the sea bottom by vertical mooring lines in tension. A semi-submersible is a similar structure, but it is held down by slack mooring lines. On the other hand, a spar floating platform is a large vertical cylinder, held down to the sea floor by slack or taut mooring lines. The cylinder provides buoyancy to keep the spar afloat and can also be used to store oil. The spar considered here has a center well that encloses the production risers. This provides for additional protection and easier maintenance

of the production risers.

The mooring lines are typically designed so that the resonance periods of these large-volume structures are outside the dominant wave energy periods. For example, resonance periods in the horizontal direction of the spar can be of the order of 5 minutes, far above the wave periods that may be around 5 to 15 seconds. In this study, we will analyze these long-period responses in the wave direction, often referred to as slow-drift responses, for a spar platform and compare model predictions to wave tank measurements. Similar models have been applied before to TLPs [18] and will be extended here for the spar platform. The large slow-drift motions seem to be critical in various design aspects of the spar and the model can, generally, be extended to analyze other motions of the spar as well.

The spar platform is a relatively new concept (compared to TLPs, for example) and the few studies done before [11, 12, 15, 21] do not seem to systematically compare model predictions to wave tank data in random seas. In this study, we strive to apply different hydrodynamic models and systematically compare time domain predictions (using measured waves) to the measured response time histories in random seas. The response here refers to the horizontal displacement measured near the spar deck in irregular random waves.

Note that this study is part of the doctoral studies of the author and this report has largely been adapted from the author's thesis [4]. The published paper [5] on this work is attached in Appendix C for reference.

Chapter 2

Spar Model for Slow-drift Response

2.1 Experimental Data

The floating structure chosen for this study, shown in Fig. 2.1, is a catenary-moored spar buoy, intended for deep-water production and storage. The important properties required in modeling the spar are summarized in Table 2.1. A 1:55 model scale of the spar was tested in the OTRC wave tank [14] under various wave conditions. We will look here at the random sea simulations of waves and resulting displacements in the horizontal along-wave direction. To investigate these motions, we will need to look at surge and heave displacements, pitch rotations and airgap measurements (see Fig. 2.2) in the wave tank. If the MWL is the origin, surge is defined to be horizontal displacement along the wave direction at the MWL. Pitch rotation is the rotation of the spar measured at the MWL in the plane of wave direction. Finally, heave is the vertical motion of the spar.

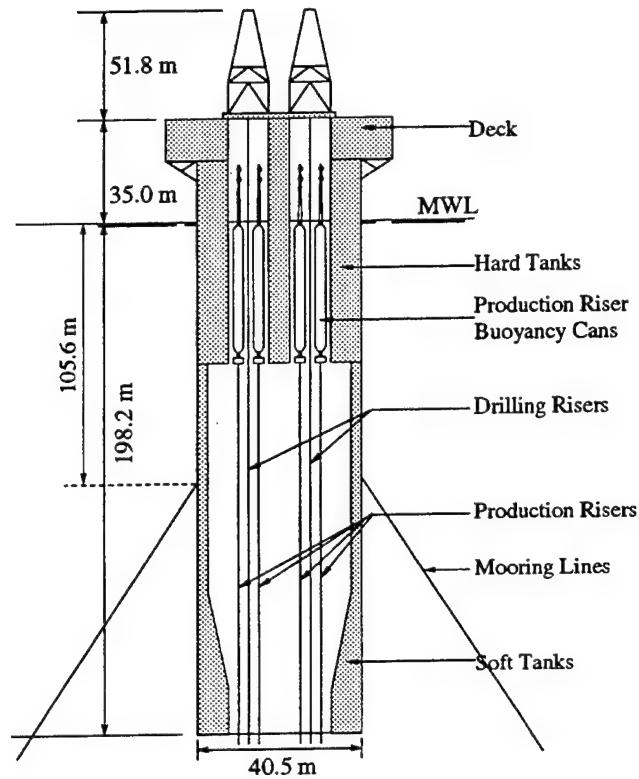


Figure 2.1: Elevation view of Spar platform

Table 2.1: Details of the spar configuration (in prototype scale)

Description	Notation	Value
Diameter	D	40.5 m
Draft from Mean Water Level (MWL)	H	198.2 m
Mass with entrapped water	m	2.59×10^8 kg
MWL to Center of Gravity	Z_{CG}	105.8 m
MWL to Center of Buoyancy	Z_{CB}	99.1 m
MWL to mooring connection	Z_f	105.6 m
Radius of gyration wrt MWL	K_r	122.8 m
Mooring stiffness in horizontal direction	k	191 kN/m
Measurement gauge location above MWL	Z_m	54.8 m
Water Depth	d	922 m

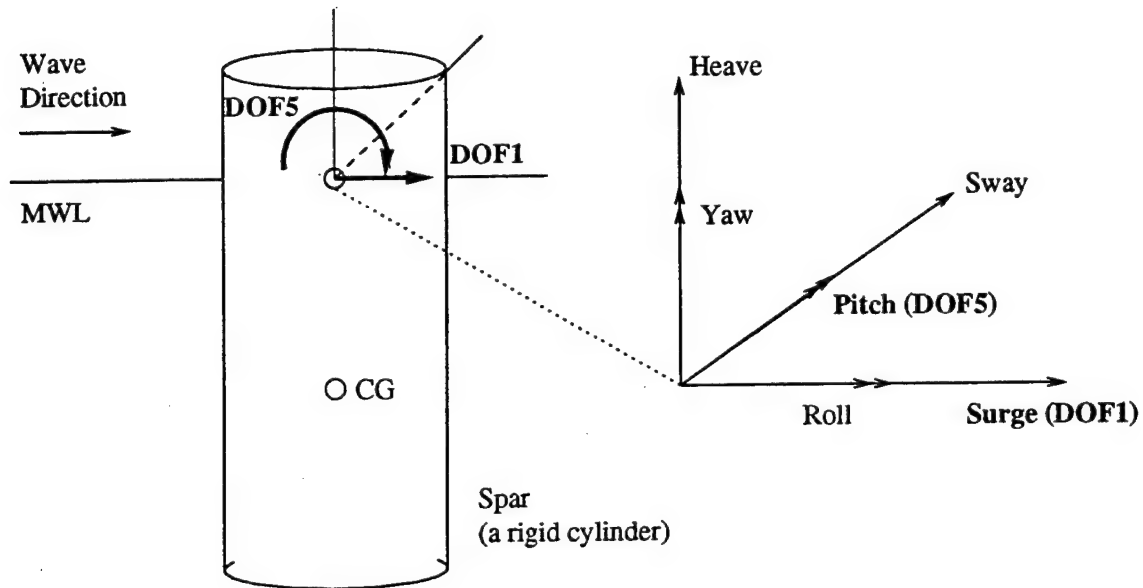


Figure 2.2: Degrees of freedom for spar

In the wave tank, the spar was tested for the following wave conditions:

- 12 different regular waves
- 14 different combinations of bi-chromatic waves
- 4 different random wave seastates
- various tests for combinations of random waves, currents and variable winds

The random wave measurements are for durations of one hour each with a sampling frequency of 0.37 seconds, and simulate the following storms:

- operational and installation seastates, both long-crested and short-crested
- a 10-year Gulf of Mexico storm
- a 100-year Gulf of Mexico storm

- a North Sea storm
- a West Africa storm

Of these, we focus on the two most severe storms: (1) the 100-year Gulf of Mexico, and (2) the North Sea storm. The experiments include two different hourly realizations of the same Gulf of Mexico storm and one hourly realization of the North Sea storm. The remaining smaller storms are not considered in this study. A summary of the wave tank measurements in the two storm is:

- two realizations (1 hour each) of a seastate described by a JONSWAP spectrum with significant wave height $H_s = 13.1\text{m}$, $T_p = 14\text{s}$, and a peakedness factor $\gamma = 2.0$. These seastates are intended to represent roughly 100-year H_s conditions in Gulf of Mexico sites and we will refer to these tests as GOM1 and GOM2
- one realization (of 1 hour) reflecting a second seastate characterized by $H_s = 14\text{m}$, $T_p = 16.3\text{s}$, and $\gamma = 2.0$. This seastate roughly represents 100-year H_s conditions in the North Sea and we will refer to this test as NS.

In these experimental tests, the surge and heave responses are recorded by a video camera tracking a light source placed 54.8 meters above MWL along the cylinder vertical axis. The pitch rotations were recorded by an inclinometer mounted on the deck of the model. The airgap measurements were recorded by a probe attached to the spar deck facing the waves, while another probe measuring the wave surface was placed 125 meters (prototype scale) away from the spar, in a direction perpendicular to the propagating waves. This probe placed away from the spar is intended to measure the undisturbed waves, or what is typically referred to as the "reference" waves. The airgap probe measures the "disturbed" waves, which refers to the waves in the presence of a structure.

Table 2.2: Reference wave summary statistics for the OTRC wave tank tests used for slow-drift response analysis of the spar

Test	GOM1	GOM2	NS
Npts	9702	9702	9702
Nominal H_s (m)	13.1	13.1	14
Nominal T_p (m)	14	14	16.3
Observed H_s (m)	14.15	13.98	14.78
Observed T_p (sec)	14.1	14.1	16.1
Calculated T_z (sec)	10.83	10.74	12.0
Mean, μ (m)	.063	.076	-.040
Sigma, σ_η (m)	3.537	3.495	3.699
Skewness, α_3	0.307	0.309	0.173
Kurtosis, α_4	3.057	3.242	3.277
Minimum (m)	-9.054	-9.711	-11.12
Maximum (m)	12.74	16.21	17.52

A summary of the reference wave statistics, as found from the measurements, is reported in Table 2.2. The observed H_s is defined to be four times the wave σ_η , while the observed T_p has been found from an averaged spectrum from the measured wave histories. $T_z = \sqrt{\lambda_0/\lambda_2}$ is found from second (λ_2) and zeroth (λ_0) moments of wave spectrum $S(f)$ with no smoothing, where $\lambda_n = \int f^n S(f) df$. Note the presence of nonlinearities in the waves ($\alpha_3 > 0$ and $\alpha_4 > 3$), and the differences in the target (nominal) and observed H_s values.

In the response measurement we focus here on the surge displacement of the spar. These slow-drift responses in the surge direction are usually large and can govern the design of many structural elements, for example the mooring lines, of the spar. The heave response for a spar platform is comparatively small and will not be investigated in this study. We anticipate no significant roll, sway or yaw motions to occur in unidirectional seas for this axi-symmetric structure and will not study

these motions either. For the spar considered here, the horizontal displacement is measured at an elevation of 54.8 m above the MWL. Since this measurement point is away from the center of rotation, the horizontal displacement will be contributed by the surge displacement and the pitch rotation (about the center of rotation). Note that the center of rotation is close to the center of gravity of the spar. If we define the rigid-body degrees of freedom (DOF) at the MWL (see Fig. 2.2), then a unit radian pitch rotation will cause a 46 meter ($= 54.8 \times \sin(1)$) displacement in the horizontal direction at the measurement point. We will refer to surge-induced displacement as "DOF1 displacement", and the pitch-induced displacement at the measurement point as "DOF5 displacement".

To understand these surge- and pitch-induced displacements, we will look at one of the measured horizontal displacements. Figure 2.3 shows the power spectrum of the measured horizontal displacements for GOM1. This spectrum shows three prominent peaks which in sequence left to right are: the surge-induced, the pitch-induced and the wave-frequency components. Note how small the wave-frequency contribution (around $f=0.07$ seconds $\approx 1/T_p$) is compared to the other two components. The surge and pitch components appear to contribute more to the total horizontal displacement.

The peaks in the spectrum indicate natural periods in surge (DOF1) and pitch (DOF5) to be about 330 and 70 seconds, respectively. Independent free decay tests of this spar also indicate the natural periods in surge and pitch to be about 330 and 67 seconds [14]. To study the three components separately, we introduce frequency cutoffs at 0.006 Hz and 0.03 Hz to filter the contributions from the three components. The frequency range below 0.006 Hz indicates the surge component, and the range above 0.03 Hz indicates the wave-frequency component. Finally, the pitch-component range is assumed to be between 0.006 Hz and 0.03 Hz.

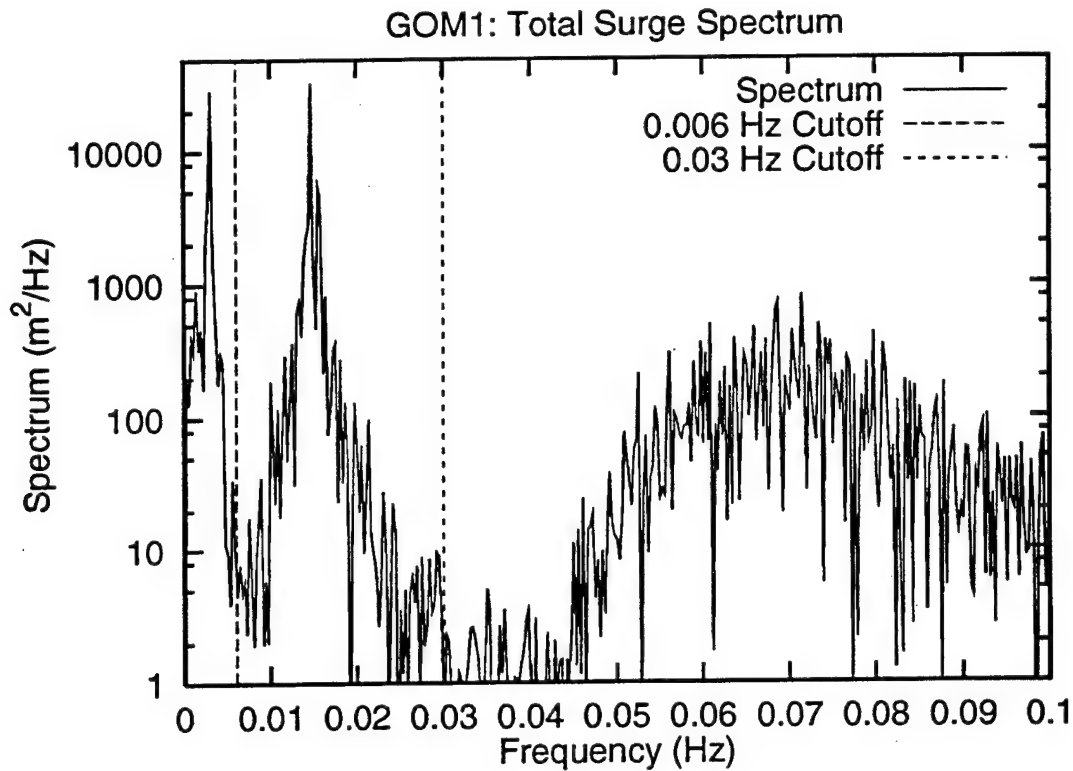


Figure 2.3: Spectrum of measured surge displacements at 54.8m elevation above MWL for GOM1 seastate

Table 2.3 summarizes the statistical moments of the horizontal displacement histories, and the moments of its filtered components is presented in Table 2.4. A comparison of standard deviations σ of filtered components in the three measurements, confirms that compared to the wave-frequency component, the low-frequency or slow-drift components (DOF1 and DOF5) dominate the total horizontal displacement. Thus a force model capturing only the wave-frequency components is likely to severely underpredict the horizontal displacements. Such a force model is usually referred to as a linear or a first-order model. For example, in Fig. 2.3 a linear force

Table 2.3: Statistical moments of the measured horizontal displacements for the seastates. Note that the maximum and minimum values contain μ .

Seastate	μ (m)	σ (m)	α_3	α_4	Min.(m)	Max.(m)
GOM1	4.942	5.788	0.078	2.677	-12.32	22.76
GOM2	5.130	6.176	0.052	2.965	-14.95	25.99
NS	3.396	7.949	0.144	3.163	-21.87	29.35

Table 2.4: Statistical moments of the filtered components (with zero mean) of measured horizontal displacements

Component	σ (m)	α_3	α_4	Min.(m)	Max.(m)
GOM1					
Wave-frequency	2.473	-0.023	2.697	-7.882	7.158
Surge component	3.375	0.091	2.196	-6.378	7.229
Pitch component	3.997	-0.005	2.177	-9.733	9.520
Surge+Pitch Comp.	5.233	0.044	2.443	-8.466	18.52
GOM2					
Wave-frequency	2.508	-0.032	2.843	-7.933	7.604
Surge component	3.937	0.185	2.959	-8.818	10.24
Pitch component	4.040	-0.002	2.357	-9.516	9.854
Surge+Pitch Comp.	5.643	0.026	2.968	-11.94	20.77
NS					
Wave-frequency	3.159	0.028	3.006	-10.36	11.32
Surge component	4.373	-0.113	2.051	-8.938	7.897
Pitch component	5.906	-0.077	2.625	-18.57	15.38
Surge+Pitch Comp.	7.356	0.048	3.094	-17.05	26.12

model would attempt to predict only the wave-frequency component, and it would fail to predict the DOF1 and DOF5 components. Another force model that, instead, attempts to predict the force components away from the wave-frequency region is often referred to as a second-order model. In general, a second-order model includes forces that are at the sums and differences of the wave frequencies. In modeling the

high-frequency heave response of a TLP, for example, interest focuses on the sum-frequency component, while in this study where the slow-drift response is of interest, a difference-frequency model would be more appropriate. Recall that in modeling the wave elevations [3], we needed both the sum- and difference-components.

We will next look at the component time histories in Fig. 2.4. The vertical axis label in each plot indicates the component being displayed. For the total horizontal displacement (shown in the topmost plot in Fig. 2.4), note the distinct transition in response characteristics around 1500 seconds. The displacement prior to 1500 seconds seems to be due to dominant pitch motions, while after 1500 seconds the surge-induced (low) frequency response seems more dominant. This is also evident in the time history components shown, where the surge amplitudes are larger in the second half hour than in the first. Such a transition shows the difficulty in modeling a seemingly non-stationary behavior of the spar. The very limited number of surge response cycles seen in the hourly measurement additionally contribute to the difficulty in calibrating a model to this data. In this study, we investigate four such model forms that attempt to capture the nonlinear forces and the resulting responses of the spar. The model predictions will be compared to the wave tank measurements. Note that in these models, while the forces can be nonlinear, the structure is still assumed to respond linearly to the incident forces.

2.2 Structural Model

As mentioned earlier, the surge displacement, measured at an elevation of 54.8 m above the MWL, is contributed by the surge and pitch DOFs defined at the MWL. In order to capture this dual-contribution to the total horizontal displacement, we model

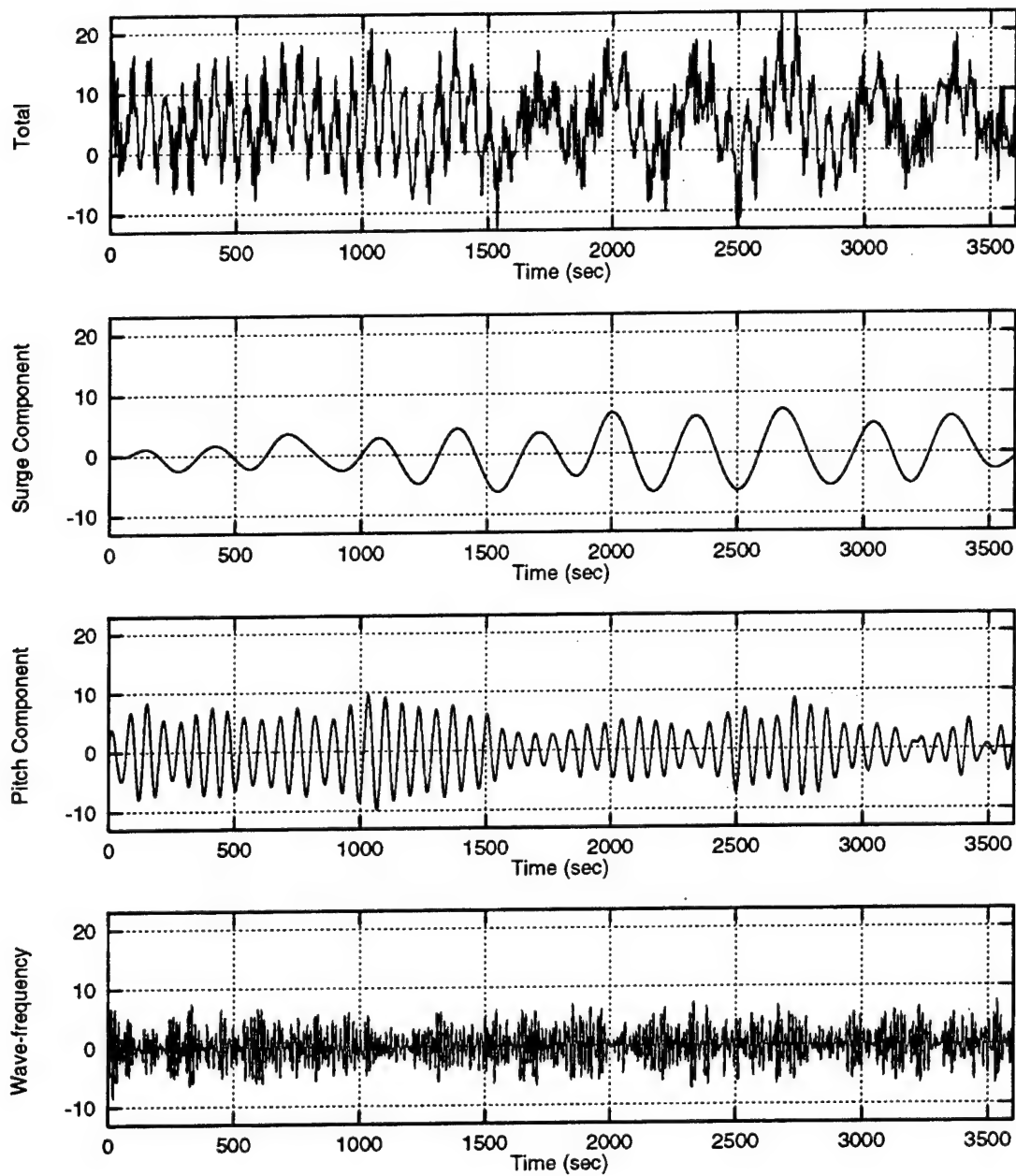


Figure 2.4: Total measured horizontal displacement and its filtered surge, pitch and wave-frequency components for GOM1 seastate

the spar as a rigid cylinder with two DOFs (surge and pitch) defined at the MWL, see Fig. 2.2. To define the DOFs we choose the MWL as the origin because the first- and second-order waves forces have been defined with the MWL as the origin. Note that the spar is modeled as a rigid body, and the surge and pitch DOFs or modes refer to the rigid body motions of the spar close to the surge and pitch resonance frequencies.

From geometry considerations, we find that the structural mass matrix M_{str} , from properties summarized in Table 2.1, for the 2-DOF model is

$$\begin{aligned} M_{\text{str}} = \begin{bmatrix} m_{11} & m_{15} \\ m_{51} & m_{55} \end{bmatrix} &= \begin{bmatrix} m & -mZ_{CG} \\ -mZ_{CG} & I(=mK_r^2) \end{bmatrix} \\ &= \begin{bmatrix} 2.59 \times 10^8 \text{kg} & -2.74 \times 10^{10} \text{kg.m} \\ -2.74 \times 10^{10} \text{kg.m} & 3.91 \times 10^{12} \text{kg.m}^2 \end{bmatrix} \end{aligned} \quad (2.1)$$

The added mass matrix M_{add} , reflecting the effects of waves radiated by the oscillating spar, is assumed to be constant for the low-frequency modes, and is found from diffraction analysis [8] to be

$$M_{\text{add}} = \begin{bmatrix} 2.71 \times 10^8 \text{kg} & -2.60 \times 10^{10} \text{kg.m} \\ -2.60 \times 10^{10} \text{kg.m} & 3.20 \times 10^{12} \text{kg.m}^2 \end{bmatrix} \quad (2.2)$$

Note that M_{add} is of the same order of magnitude as M_{str} for this large-diameter structure. The stiffness matrix, again from geometry considerations, is found to be

$$K = \begin{bmatrix} k & -kZ_f \\ -kZ_f & kZ_f^2 + k_h \end{bmatrix} \quad (2.3)$$

where k_h is the hydrostatic stiffness encountered by the spar when rotated in the

pitch direction, and is given for small rotations as [12]

$$k_h = \pi R^2 H \rho g (Z_{CG} - Z_{CB}) - \frac{\pi}{4} \rho g R^4 \quad (2.4)$$

where ρ is the water density, g is the acceleration due to gravity and $R = D/2$ is the spar radius. On substituting these, we find

$$K = \begin{bmatrix} 1.91 \times 10^5 \text{N/m} & -2.02 \times 10^7 \text{N} \\ -2.02 \times 10^7 \text{N} & 1.6 \times 10^{10} \text{N.m} \end{bmatrix} \quad (2.5)$$

An eigenvalue analysis of the 2-DOF spar is solved for the shapes Φ and squared frequencies Λ using

$$K\Phi = M\Phi\Lambda \quad (2.6)$$

in which $M = M_{\text{str}} + M_{\text{add}}$ and Λ is a diagonal matrix of the squared frequencies and results in the natural surge and pitch periods of 331 seconds and 69.9, respectively. This is very close to the natural periods observed for the GOM1 seastate (see Fig. 2.3) and also close to the natural periods found from the free decay tests. This confirms the modeling of the mass and stiffness properties. The eigenmodes, scaled to unit values in the DOFS,

$$\Phi = \begin{bmatrix} 1 & 100.6 \\ 6.8 \times 10^{-5} & 1 \end{bmatrix} \quad (2.7)$$

indicate the first mode of the cylinder to be surge dominated, while second mode shows a 100.6 meter horizontal displacement for every unit radian rotation in pitch. Note that this system shows strong “geometric-coupling” induced by the distance from measurement point to the center of rotation.

2.3 Hydrodynamic Model Forms

The base case model considered here for the spar is a linear, 2-DOF (DOF1 and DOF5) rigid cylinder with incident wave forces estimated from diffraction analysis of the structure [8]. The diffraction analysis for any structure is commonly done by applying sinusoidal waves of different frequencies ω_k chosen from the wave power spectrum. Irregular waves can be written as $\eta(t) = \text{Re} \sum C_k \exp(i\omega_k t)$ where C_k are complex Fourier amplitudes. The first-order forces $f_1(t)$ are then found at these incident wave frequencies as

$$f_1(t) = \text{Re} \sum C_k H_1(\omega_k) \exp(i\omega_k t) \quad (2.8)$$

where H_1 is the first-order transfer function, while the second-order forces are found as the forces at pairs of wave frequencies as

$$f_2(t) = \text{Re} \sum \sum C_m C_n H_2^-(\omega_m, \omega_n) \exp[i(\omega_m - \omega_n)t] \quad (2.9)$$

where H_2^- is referred to as the difference-frequency transfer function.

Note that in finding these transfer functions through second-order diffraction analysis, the spar was allowed to float freely [8, 9]. A linear diffraction analysis was used to estimate the frequency-dependent added mass and damping for the spar. Note that the second-order diffraction analysis is computationally intensive and limited to a few wave frequency pairs (here 8×8 frequency grid ranging from 0.2 to 1.18 rad/sec.). We adopt a surface spline fitting scheme FITQTF [7] to interpolate the sparse QTF to a fine mesh for use in predictions using TFPOP [17]. See Appendix B for some studies on the sensitivity of the predicted results to different interpolation schemes.

What remains to be modeled are the damping ratios, ξ_1 and ξ_5 , of the system in the two DOFs that can be used to construct the damping matrix C of the system as

$$\Phi^{-1}M^{-1}C\Phi = \begin{bmatrix} 2\xi_1\omega_1 & 0 \\ 0 & 2\xi_5\omega_5 \end{bmatrix} \quad (2.10)$$

where ω_1 and ω_5 are the resonance periods in surge and pitch DOFs.

The damping ratios ξ_1 and ξ_5 for the 2-DOF system are calibrated using measured data. An approach for such a calibration could be to tune ξ_1 and ξ_5 such that the predicted σ matches measured σ in each mode. This approach, however, may mask potential errors in the force levels. For example, if the force levels from diffraction analysis are overestimated, then the system will end up being tuned to an overly large ξ values to compensate the large forces. Alternatively, we can tune ξ 's from the measured spectral bandwidth δ [1] in each DOF. Other methods include half-power bandwidth, or random decrement method [19]. In this study, we will use the spectral moments λ_n to estimate the bandwidths δ .

$$\delta = \sqrt{1 - \lambda_1^2/(\lambda_0\lambda_2)}; \quad \lambda_n = \int f^n S(f) df \quad (2.11)$$

where $S(f)$ is the measured spectrum. Note that δ_1 the bandwidth of the surge component is found from $S(f)$ for $f \leq 0.006$ Hz. Similarly, pitch component bandwidth δ_5 is from the spectral moments for $0.006\text{Hz} < f < 0.03\text{Hz}$. We resort to an iterative identification of the damping ratios, so that the predicted response bandwidth matches the measured bandwidth simultaneously in both DOFs.

We may additionally recognize wave-drift damping [2, 18] as another damping mechanism in the system. This damping is due to the spar (slow) drifting in the waves.

The resulting force is proportional to the spar velocity and to the wave amplitude-squared [2]. A consequence of this extra damping force is that it “clips” the peaks of the surge response, and as such is a “beneficial” nonlinearity that we will include in our second model. Wave-drift damping, similar to nonlinear force, is a second-order effect and is to be defined across pairs of wave frequencies (as in the QTF definition). In this study, the diagonal values for wave-drift damping definition were found using SWIM [10] and the off-diagonal terms estimated using Newmann’s approximation [13]. The effect of this approximation should be small for this slow-drift problem, as the interesting frequency pairs lie very close to the diagonal.

As will be demonstrated in the comparisons to follow, we see that both of these models appear to underestimate the value of the most basic indicator of nonlinearity: the net mean applied force and hence the observed mean horizontal displacement. This mean underprediction may be due to the absence of viscous forces in the models. An asymmetry in the viscous forces, due to the effect of integrating to the time-varying surface, causes a net mean offset of the structure in the wave direction. A third model is thus considered that additionally includes viscous force effects. The viscous forces are found as Morison’s drag force integrated from the spar bottom (keel) to the free surface. The drag force is based on absolute fluid velocity with an assumed coefficient of drag $C_D = 0.6$ to reflect large viscous effects in a wave tank. A Wheeler stretching [22] of the water particle kinematics is used above the mean water level.

It may be argued that the disturbed waves, instead of the reference waves (as used in the third model) better represent the wave surface close to the cylinder and as a result will capture the viscous forces effects more appropriately. Recall that the disturbed waves have been measured in the wave tank by a wave probe attached to

Table 2.5: Nomenclature for the four proposed model forms

	Description	Model
1	Base-case model with diffraction forces	DF
2	Model with diffraction forces and wave-drift damping	DF/WDD
3	Model with diffraction forces, wave-drift damping and viscous forces from reference (undisturbed) waves	DF/WDD/VF(u)
4	Model with diffraction forces, wave-drift damping and viscous forces from disturbed waves	DF/WDD/VF(d)

the deck of the spar. Inclusion of viscous forces from disturbed waves leads to the formulation of a fourth model. We will compare predictions from these four models in the following sections. Reference will be made to the models by names as given in Table 2.5.

2.4 Input Wave Histories for Models

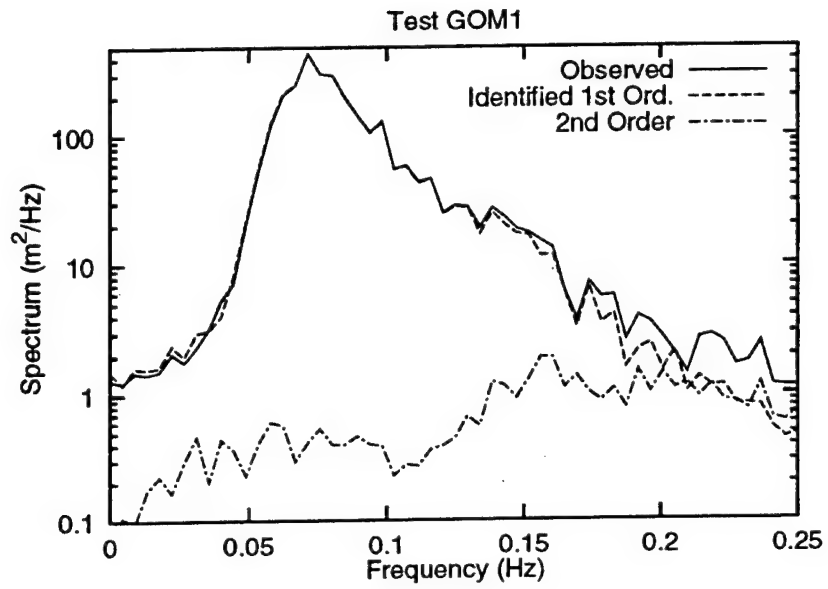
To consistently use the LTFs and QTFs from the diffraction analysis, which assumes the input waves to be Gaussian, we seek to infer consistent first-order wave components from the measured reference waves. We will apply these first-order waves to estimate the diffraction forces on the spar. We use WAVEMAKER [6] to identify the first-order components of the reference waves for each of the three seas: GOM1, GOM2, and NS. The methodology to identify the underlying first-order waves is to seek the implied first-order wave history that, when run through the second-order wave predictor, yields an incident wave that agrees with the target observed history at each time point. This identification is performed using a Newton-Raphson scheme

to achieve simultaneous convergence at each complex Fourier component. Details of this identification scheme can be found in Appendix A. Figure 2.5a shows a comparison of the reference wave spectrum for GOM1 seastate being studied here and the identified underlying first-order wave spectrum. Note that, as observed in Reference [3], the spectral density of the second-order component is significantly smaller (even at twice the peak spectral frequencies) than that of the first-order component, however, phase locking of the first- and the second-order component (see Fig. 2.5b) leads to larger crests and flatter troughs.

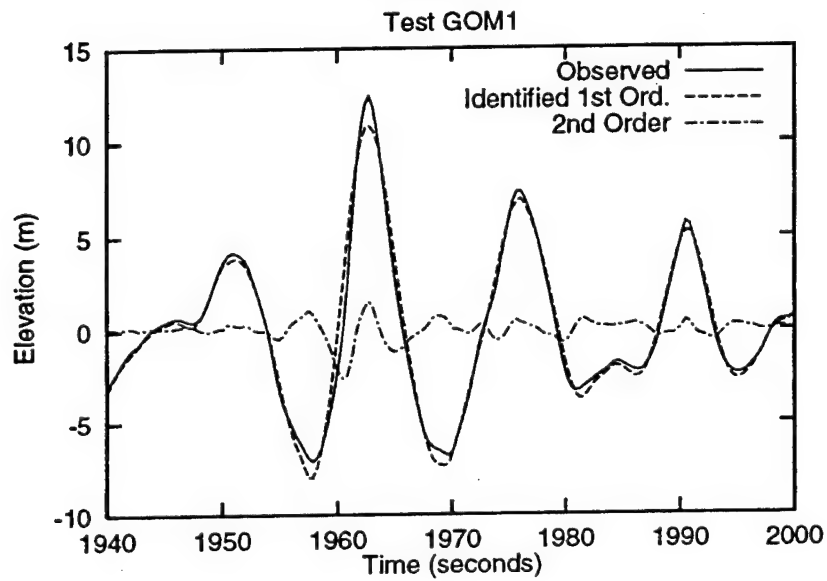
In the DF/WDD/VF(u) model, while diffraction forces are still based on the underlying first-order waves, viscous forces are based on the observed reference waves. In the DF/WDD/VF(d) model, viscous forces are based on the disturbed waves as measured by the airgap probe attached to the spar. Note that the airgap probe, measuring the free surface elevation above the still water level, includes the heave (vertical) motions of the spar. We compensate the airgap measurements for these heave motions to get the time-varying free surface. This inferred wave time history is referred to as disturbed waves.

2.5 Calibrated Damping Values

As proposed, we iteratively identify the damping ratios ξ_1 and ξ_5 in surge and pitch DOFs, so that the predicted spectral bandwidths in each frequency component simultaneously match measured results. Since GOM1 and GOM2 are two realizations of the same seastate, we find common damping ratios across the seastates for each mode. We do this by tuning ξ_1 and ξ_5 so the bandwidths δ_1 and δ_5 of the predicted spectrum that has been averaged across the two seastates, match simultaneously the



(a) Wave Spectrum



(b) Wave History near maximum crest over one hour test

Figure 2.5: Reference (observed) wave vs. underlying first- and second-order waves

Table 2.6: Calibrated damping ratios (%), ξ , for the models in surge (DOF1) and pitch (DOF5) components

Model	GOM1 & 2		NS	
	Surge	Pitch	Surge	Pitch
DF	4.5	1.6	1.7	.001
DF/WDD	3.3	0.6	.001	.001
DF/WDD/VF(u)	4.0	0.5	2.5	.001
DF/WDD/VF(d)	6.5	.001	0.1	.001

bandwidths of the observed spectrum which also has been similarly averaged across the two seastates. Table 2.6 summarizes the calibrated ξ 's for the four models.

Note that if we sought to estimate damping ratios by matching the rms of the response we would expect the damping ratios from the DF/WDD models to be smaller than those of the DF models. We would similarly expect the damping ratios from the VF models to be larger than the WDD model. This is not guaranteed since we are matching the spectral shape (bandwidth); it is comforting, however, to still see this comparison in the damping ratios. For the NS case, we find that even with $\xi_5 \approx 0$ we are still not able to match the observed bandwidth exactly and the observed bandwidth is still narrower than predicted. This may be due to limited pitch data in the 1-hour measurements or there may be some effects that the model is not able to predict in the pitch motions. This may be the cause for inability of the model to match the noisy bandwidth estimates.

2.6 Estimation of Initial Conditions

Finally, we observe the need to include measured initial conditions in our prediction results. Note that a 1-hour measurement includes only about 10 ($\approx 3600/331$) response cycles in DOF1. Note also the time variation of the relative contributions of the surge and pitch components in the different parts of the time history in Fig. 2.4. In the experiments, the measurements were recorded after about 15 minutes (prototype scale) when the wave tank conditions were deemed to have achieved steady-state conditions and hence the spar is not initially at rest. In order to include transient effects and to model these few cycles appropriately, we include measured initial conditions in the predictions. If, instead, the structure were assumed in the prediction to be start from at-rest conditions, these incorrect initial conditions would corrupt the predictions, more so in DOF1 response (where we see only a few cycles) than in DOF5 (where we see about $50 \approx 3600/69.9$ cycles).

In order to estimate the initial conditions in the surge and pitch DOFs in each seastate, we need to use the measured horizontal displacements and the measured pitch rotations. The measured horizontal displacement is filtered to obtain the zero-mean surge and zero-mean pitch components. The mean offset is directly found from the measured history prior to imposing any filters. This mean contains the mean offset due to both surge and pitch components. A separate measurement of the pitch rotations is used to find the mean pitch rotation which then is converted to a mean offset due to pitch rotation. Given this pitch mean, we subtract it off from the total horizontal mean offset to get the mean offset due to surge. We add the mean surge and mean pitch offsets back into the filtered zero-mean surge and pitch histories. The initial displacement and velocity in surge DOF is then found from the first two time points of this mean-corrected surge history. Similarly, we find the initial displacement

Table 2.7: Estimated initial conditions in surge and pitch DOFs for the three seastates

Sea	Surge DOF		Pitch DOF	
	Displ. (m)	Vel. (m/s)	Displ. (rad.)	Vel. (rad/s)
GOM1	6.09	0.0135	0.188	0.00152
GOM2	4.46	-0.00951	-0.0362	-0.000694
NS	-9.22	-0.0706	-0.254	-0.00171

and velocity for the pitch DOF from the first two time points of the mean-corrected pitch history. Table 2.7 gives these estimated initial conditions at the MWL for the three seastates. Note how different they are from at rest initial conditions (zero displacements and zero velocities).

Note that the first-order response is estimated separately and does not depend on the second-order response calculation. So we, instead, efficiently predict the first-order response in the frequency domain. No initial conditions are forced on the first-order response calculation. Initial conditions will only affect the first few cycles, and will have little impact of the time histories that have hundreds of cycles.

Chapter 3

Results

To investigate the model accuracy, we will compare predicted response moments of the three frequency components: wave-frequency, surge (DOF1) component, and pitch (DOF5) component. This will give an insight into model behavior at the component level. We then will look at the combined (total) surge response to see how well the pieces fit together to yield the combined predictions, i.e., the total predicted horizontal displacement.

3.1 Wave-frequency (first-order) Response

Figure 3.1 compares the statistics of the predicted to observed first-order response. These statistics include standard deviation σ_1 , the absolute maximum response normalized by σ_1 , and the absolute maximum response. The first-order response, being primarily inertia dominated, is almost the same for all the four models. The viscous effects are accounted for in the second-order response estimation. Stiffness and damping terms contribute little to the first-order response because the natural periods are far away from the wave-frequency range (see Fig. 2.3). We see reasonable

agreement of measured and predicted σ_1 , suggesting that the mass properties, and the LTFs have been modeled adequately. The normalized absolute maximum first-order displacements from predictions also agree with observations. Note the slight overprediction for the GOM seastates in σ_1 and the normalized maximum displacements. These overpredictions combine to cause an overprediction of the absolute maximum values for the GOM seastates, as seen in Fig. 3.1. The NS first-order prediction seems to agree with observations for all three statistics.

Figure 3.2 shows time histories of the first-order response and shows good agreement in the amplitudes and phases of measurements and predictions. Note the change in the y-axis captions, when viewing Fig. 3.2. Here the 500-second windows have been shown for clarity; the rest shows similar comparison. The time window is selected to include the absolute maximum values for the observed histories. An agreement in the time histories confirms the LTF formulation from diffraction analysis and also confirms the identification of the first-order input wave components from the measured undisturbed waves. Since all the four models predict almost the same first-order response, only one predicted history is shown each of the seastates.

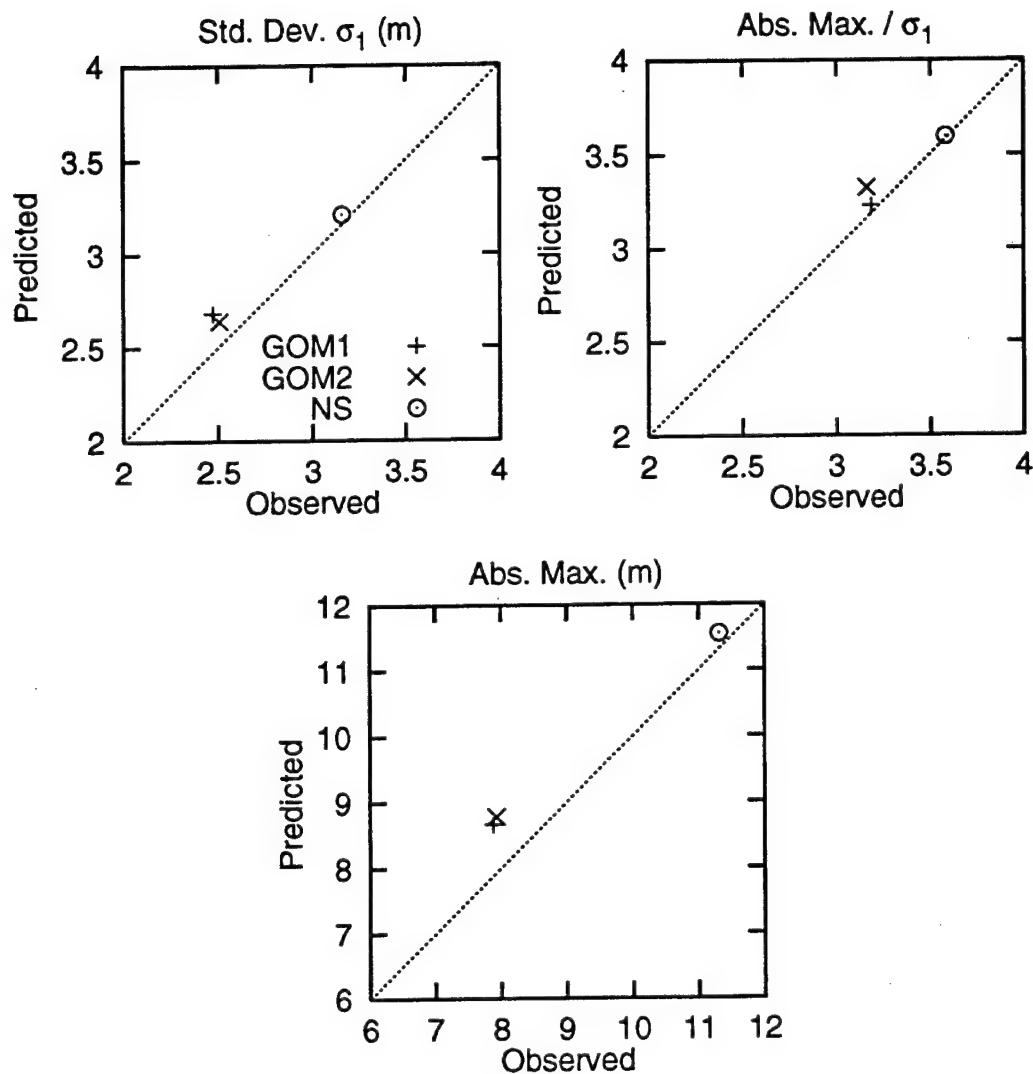


Figure 3.1: Comparison of the first-order (wave-frequency) response statistics: Standard deviation σ_1 (top left), maximum normalized by the standard deviation (top right) and absolute maximum displacements (bottom)

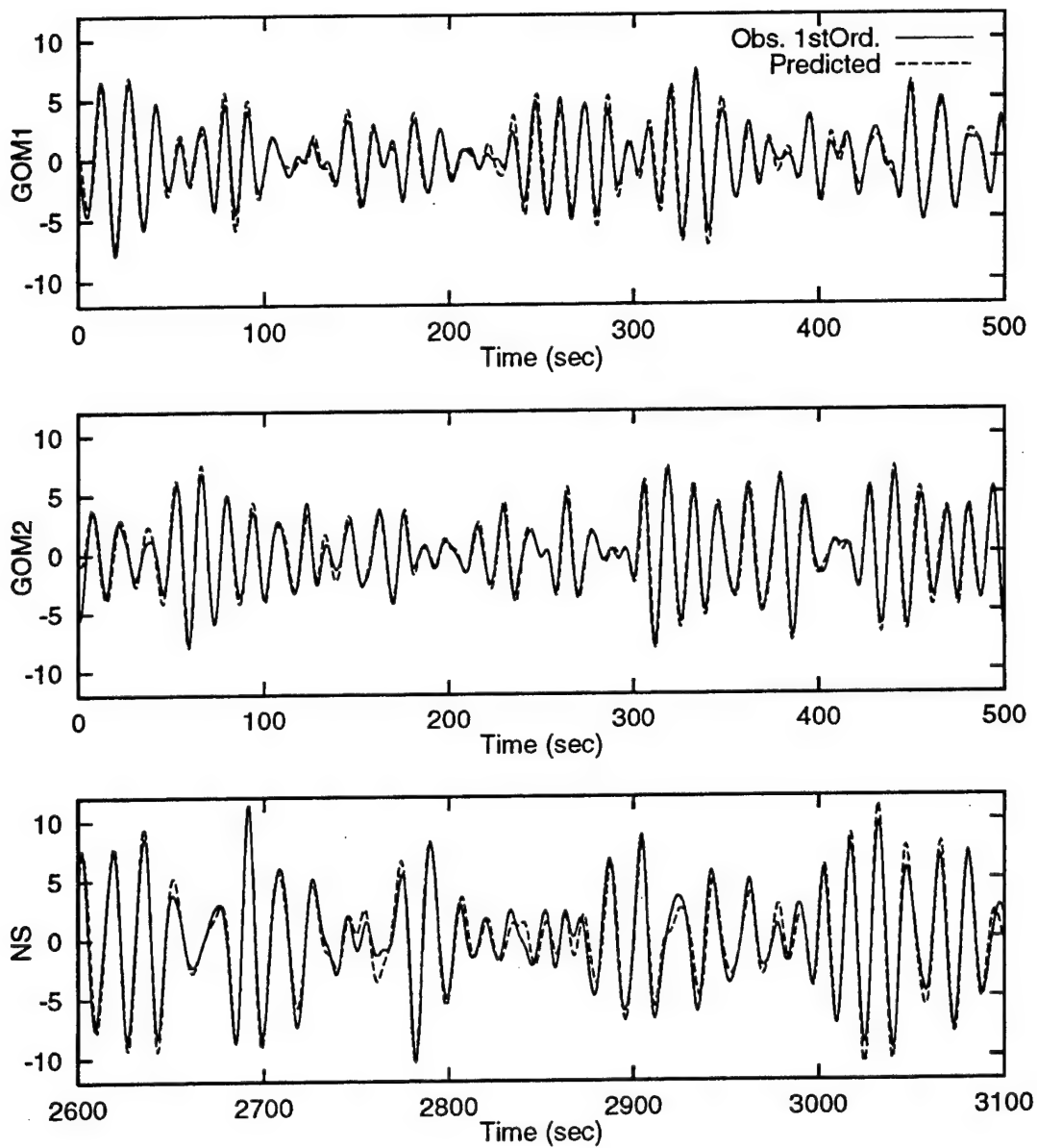


Figure 3.2: Comparison of predicted first-order response time histories to measurements across the three tests. For clarity we show only 500-second portions of each test, selected to include the absolute maximum observed response.

3.2 Surge (DOF1) and Pitch (DOF5) Component Responses

Figure 3.3 compares the predicted statistical moments to the corresponding observed values. For each moment, the observed value for each seastate appears on the X-axis, and the predicted values are shown on the Y-axis. Note that we use three symbols on the X-axis to indicate the observed values in the three seastates. See Tables 2.3 and 2.4 for numerical values of these moments. For each symbol on the X-axis, we have four model predictions each shown using a different symbol. Consequently, in one plot we should see four symbols aligned vertically, for every symbol on the X-axis, indicating four model predictions for every observed value. Each of the model predictions is shown using the same symbol across the three tests, in order to gauge the model predictions across tests. Perfect prediction is shown as a 45 degree dotted line on each plot.

As noted previously, we find here that the DF and DF/WDD models underestimate the total mean offset in surge (see Fig. 3.3). However, as also was anticipated, inclusion of viscous forces considerably improves the agreement in the predicted mean offsets. Use of disturbed waves in the VF(d) models yields, in all three tests, a slightly larger mean offset than the VF(u) model. Note that in the plot the observed mean offsets for each of the three seastates (see Table 2.3) have been marked on the X-axis (observed axis) by three different symbols. A difference in the observed values for GOM1 and GOM2 indicates the level of observed scatter to be expected when comparing model predictions to measurements.

In Fig. 3.3, a comparison of σ_{DOF1} and σ_{DOF5} , the standard deviations in the surge and pitch frequency components, shows that on average the DF model underpredicts

the rms of the response. The largest DF underprediction in σ_{DOF1} , which in the case of the NS, is about 40% of the observed value. This is also the case for GOM2. σ_{DOF5} seems only slightly underpredicted by the DF model for GOM1 and GOM2; however, σ_{DOF5} appears to be overpredicted by the DF model for the NS case. This may be due to the noisy estimate of the pitch damping ratio ξ_5 . Recall that in the NS seastate, ξ_5 is close to zero, but still the predicted spectral bandwidth was broader than observation.

In general, the underprediction in the standard deviations becomes slightly more severe on inclusion of wave-drift damping (DF/WDD model). Inclusion of viscous forces from either the disturbed or the reference waves leads to better agreement in the σ 's. From the plots, it may be argued that the VF(d) models gives better agreement in σ 's than the VF(u) model when compared across the three seastates. Note how close the VF(d) prediction is in all the three tests for both σ_{DOF1} and σ_{DOF5} , except for σ_{DOF1} in GOM2. This discrepancy for GOM2 still appears to be within the observed scatter in the rms response (difference in the rms value for GOM1 and GOM2).

Instead of comparing the predicted skewness and kurtosis values, we will directly look at the maximum response in each frequency component. We will first look at maximum displacement normalized by the rms response for each component. Note that the filtered components have zero mean in all comparisons to follow. A normalized maximum comparison will give a sense of the tail prediction by the models independent of the rms comparisons. Finally, we will look at the absolute values of hourly maximum displacements. In Fig. 3.4, the top figures compare the normalized maximum values for the two frequency components. In both the components, all predictions, in general, show good agreement with observations for GOM1 and

GOM2. In the NS case, however, surge (normalized) maximum seems to be overpredicted by almost 35% for all models. We will investigate this issue when comparing the response time histories of the surge component. Results for the absolute maximum displacements for each component can be anticipated from comparisons of the standard deviations and the normalized maximum displacements. For the maximum surge, we may anticipate that the maximum value comparisons will be similar to the rms comparison, since the normalized maximum value is well predicted in this case. The bottom-left plot in Fig. 3.4 confirms this. As may also be anticipated, the maximum response comparison in the NS case shows a large scatter in across model predictions. The underpredicted rms seems to compensate the overpredicted normalized maximum displacement in the VF(u) model so that it is closest to the observed maximum response in the NS case, while other models either underpredicted or overpredict severely the observed NS maximum surge displacement.

The bottom-right plot in Fig. 3.4, shows similar results for pitch frequency component. Here, we find the VF(d) model to yield the closest agreement to observation. The other prediction models, also yield good agreement (largest discrepancy of 12%) for the GOM seas, while they underpredict the maximum pitch response in the NS case by about 30%.

Figure 3.5 compares the measured and predicted time histories filtered to include only the DOF1 frequency range. The filtered DOF1 results for all three tests (see the Y-axis caption) along with the corresponding predictions from the DF and the DF/WDD/VF(d) models. Note how few surge (DOF1) cycles are observed in the 1-hour duration, and consequently, as noted earlier, the potential difficulty in using these few cycles to tune the prediction models. Reasonably good agreement is seen between the measured and predicted time histories for all three tests, except in the

case of the VF(d) model for NS. Note how close the predicted surge is in the GOM1 case over almost the entire duration. For GOM2 the observed surge shows a general decay in amplitude until about 1500 seconds following which we see large surge cycles. This general trend seems to be shown by both the prediction models as well. For the NS, however, the DF model prediction seems to underpredict the surge response at almost all time points and the VF(d) model seems to give better agreement with observed results. In the last two cycles, however, the VF(d) model appears to overpredict the surge amplitudes. Note that the predicted surge from either models is in phase with the observed surge, more so in the VF(d) case than in the DF case.

A comparison of the pitch (DOF5) time histories from measurement, the DF model and the DF/WDD/VF(d) model is shown in Figs. 3.6, 3.7, and 3.8. We will first focus on the GOM1 pitch histories in Fig. 3.6, where for convenience, the first half hour is shown on the top plot and the second half hour is shown in the bottom plot. A comparison of amplitudes and phases across the entire histories shows that the predicted pitch from both the models tends to generally follow the observed amplitudes, and occasionally disagrees in phase. For example, the DF model agrees with observed phase until about 1000 seconds and gradually goes out of phase around 1600 seconds and comes back in phase around 2000 seconds. The VF(d) prediction follows a similar in-out phase agreement, however, the disagreement seems less severe than the DF model. See, for example around 3000 seconds, while the DF model is completely out of phase, the VF(d) is still in phase with observation. Also, notice around 500 seconds, the VF(d) agrees with observed amplitudes much better than the DF model.

Similar, observations can also be made for the GOM2 and NS tests. It, generally, appears that the VF(d) predicted amplitudes and phases agree with observed results

better than the DF model.

Recall that we incorporate measured initial conditions for each of surge and pitch components, when predicting response. The input initial conditions for each DOF at the mean water level result in a net initial condition at the measurement point (54.8 m above the MWL). We show in Fig. 3.9, that indeed the prediction model preserves the net input initial conditions. Here we show the initial portions of the net horizontal displacement due to the surge and pitch components from observation and from prediction models: DF and DF/WDD/VF(d). Recall that the first-order or wave-frequency component is found from frequency domain analysis with no input initial conditions. Fig. 3.9 shows that we identically reproduce the net initial conditions in all the three tests and in the two prediction models. This is also true for the other two predictions not shown in this figure.

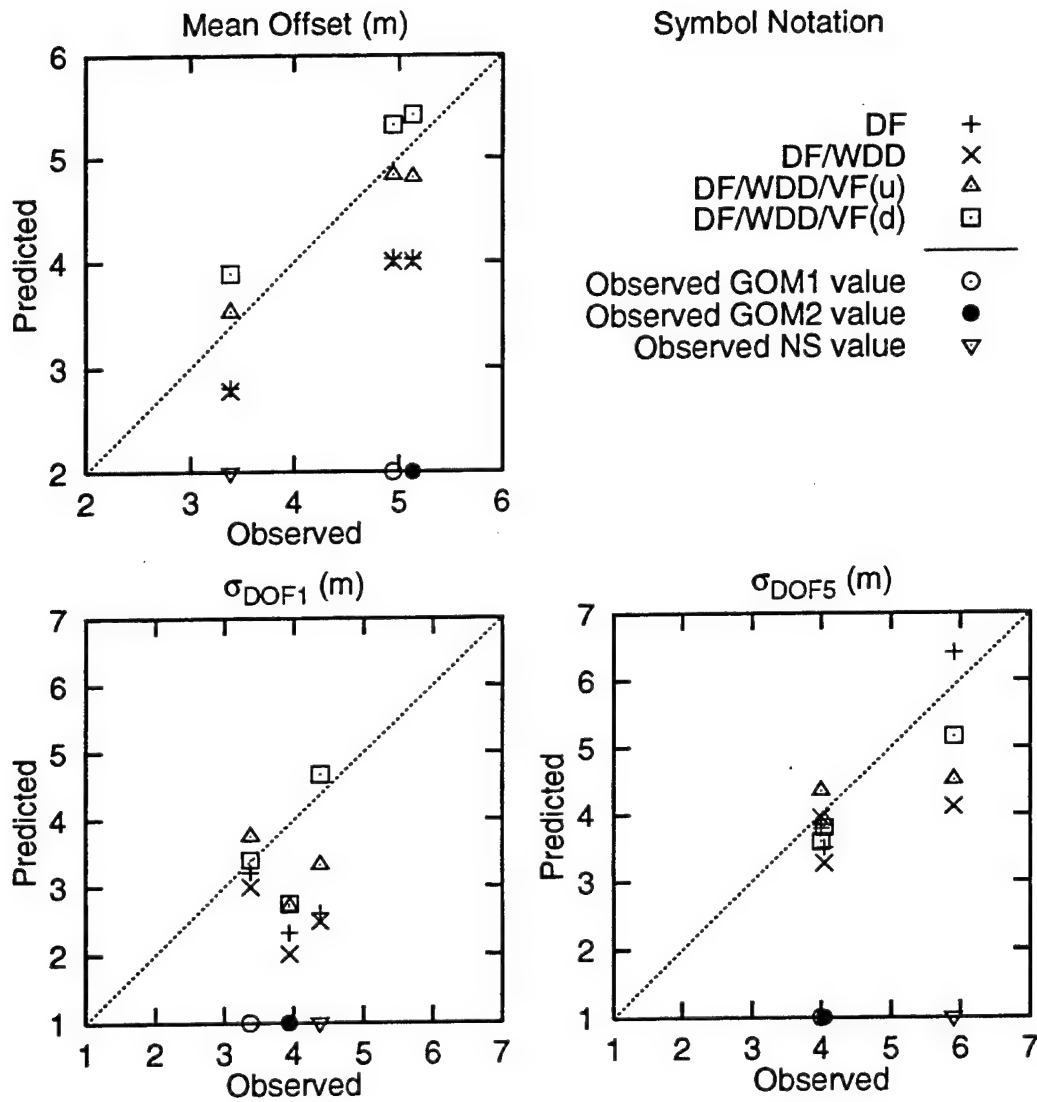


Figure 3.3: Comparison of statistical moments for surge and pitch components in the three seastates: Predictions from the four models vs. measurements. The moments include total mean, and standard deviations in surge and pitch frequency components (see titles in the figure).

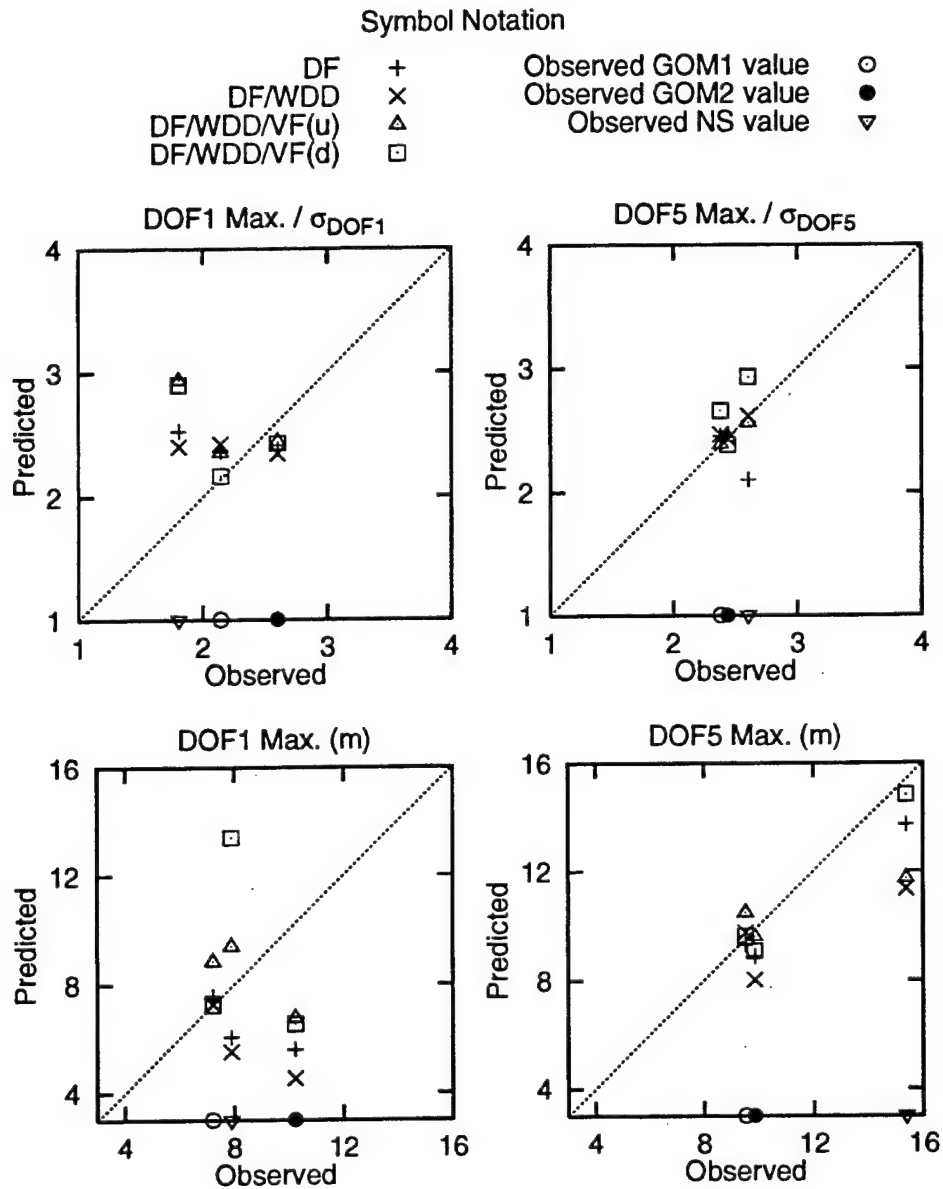


Figure 3.4: Comparison of statistical moments for surge and pitch components in the three seastates: Predictions from the four models vs. measurements. The moments include maximum normalized by the standard deviation and the absolute (unnormalized) maximum displacements in each of surge and pitch frequency components (see titles in the figure).

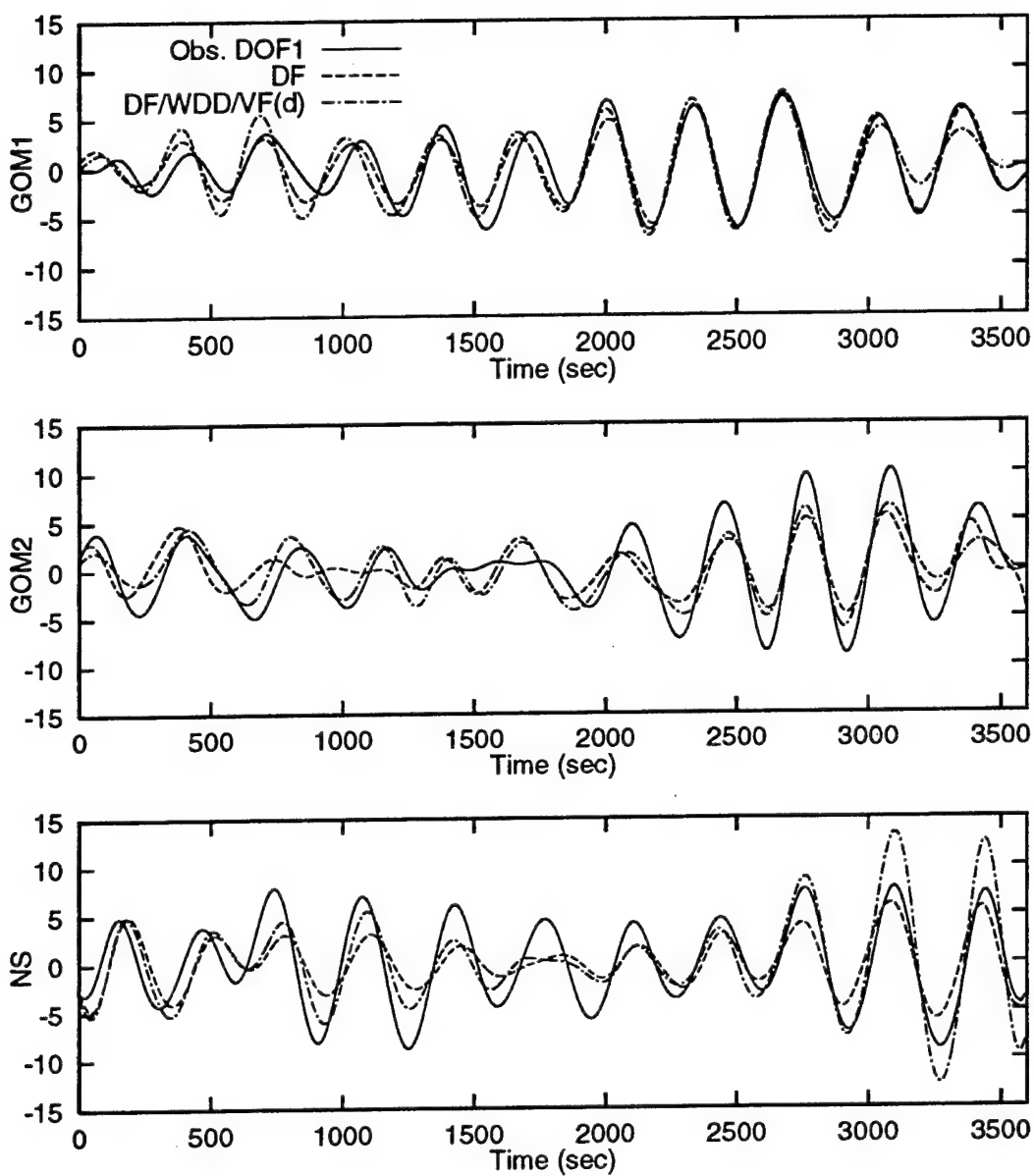


Figure 3.5: Comparison of (zero-mean) response time histories in DOF1: prediction vs. measurement

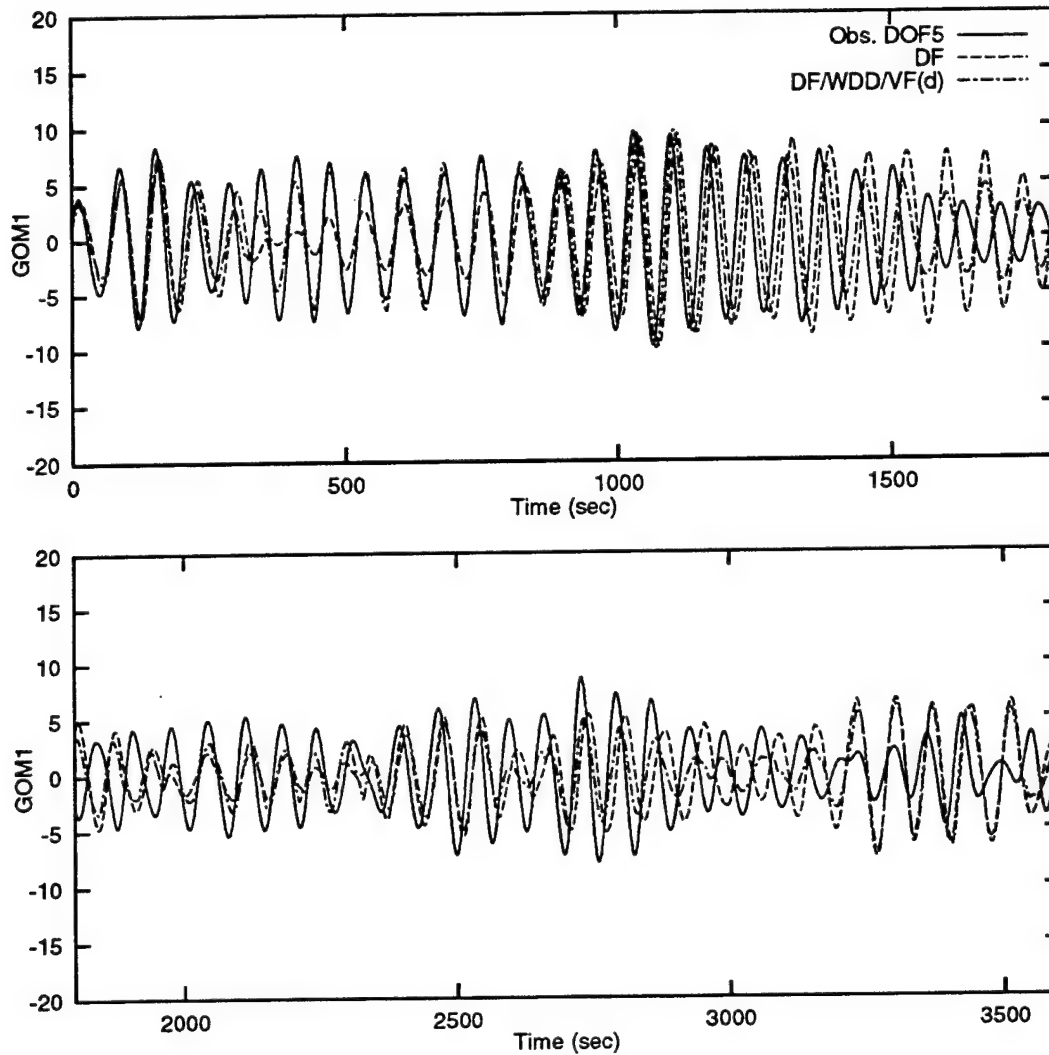


Figure 3.6: Zero-mean pitch (DOF5) time histories for GOM1: prediction vs. measurement

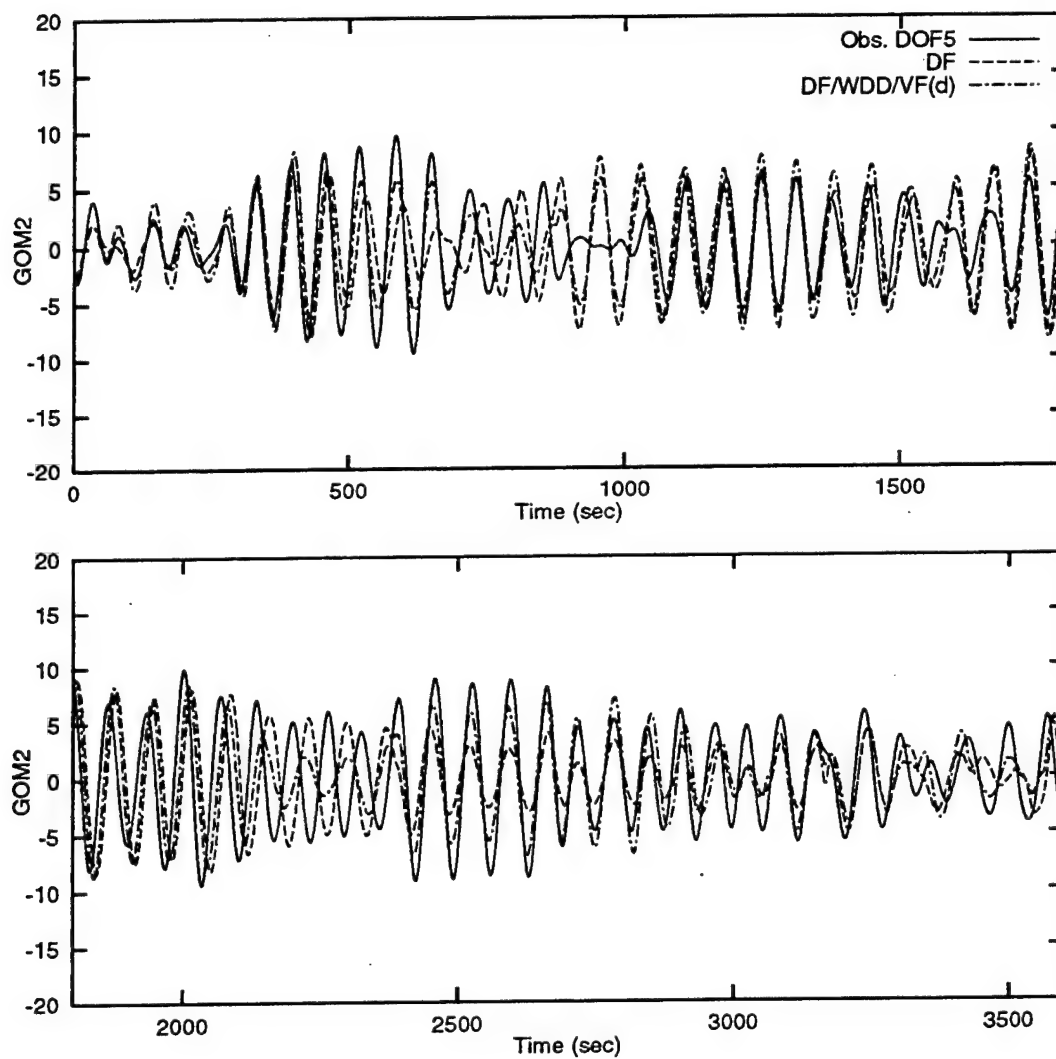


Figure 3.7: Zero-mean pitch (DOF5) time histories for GOM2: prediction vs. measurement

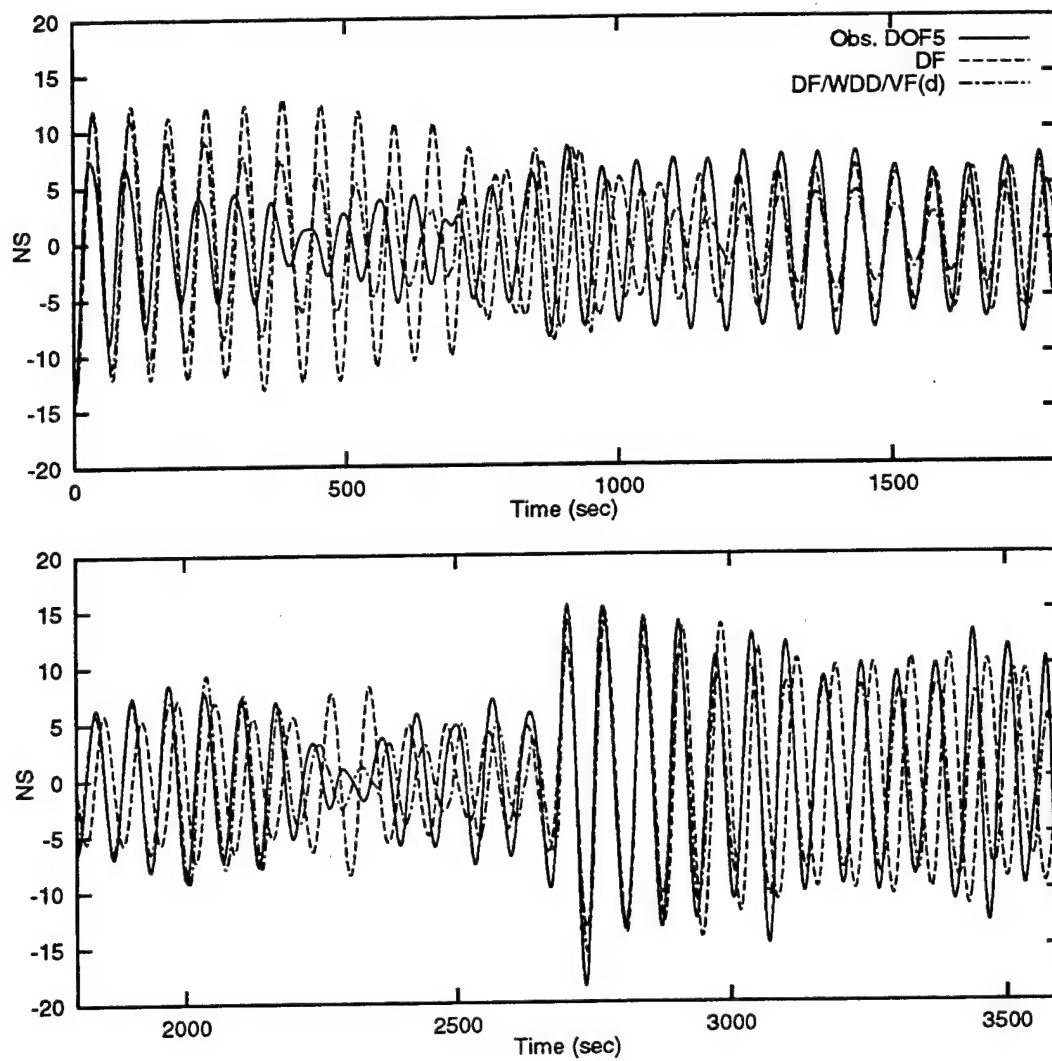


Figure 3.8: Zero-mean pitch (DOF5) time histories for NS: prediction vs. measurement

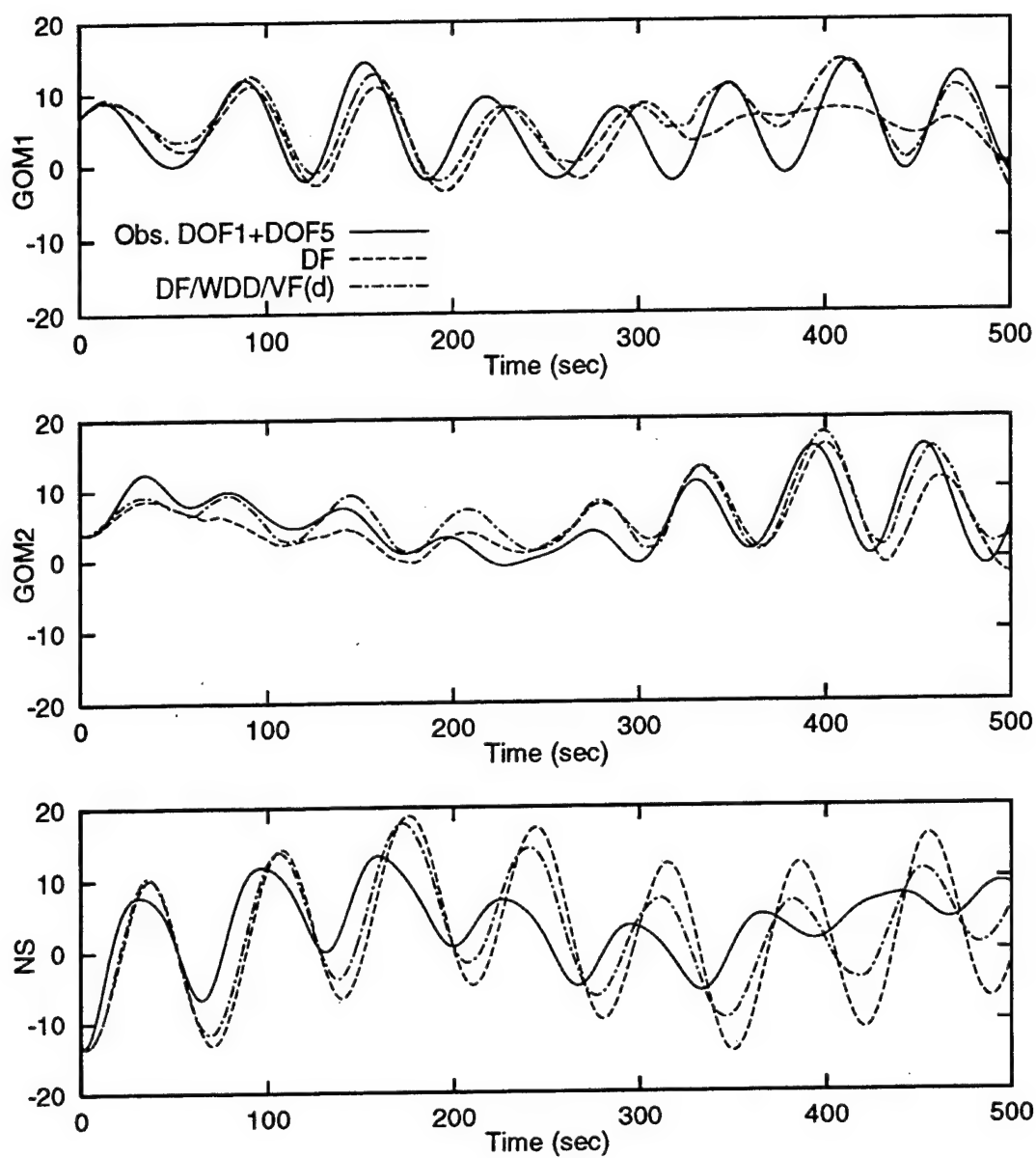


Figure 3.9: Second-order (=surge+pitch components) predicted and measured response to indicate preservation of net input initial conditions found from observed histories

3.3 Total Predicted Horizontal Displacement

Finally, we add all the predicted components together to get the total predicted horizontal displacement and compare to measurements. We add the three predicted components (wave-frequency, surge and pitch) time point by point to get a time history of the total horizontal displacement or what we may refer to as the total or combined response. Since the surge and pitch contributions to total surge response is significantly (as seen in Table 2.4) more than the first-order response, we may anticipate similar comparisons at the total response level as we did in each of surge and pitch component comparisons in Sec. 3.2. Note that the variance of the total response σ_t^2 is simply the sum of the variance of each of the three components ($=\sigma_{\text{DOF1}}^2 + \sigma_{\text{DOF5}}^2 + \sigma_1^2$). Fig. 3.10 compares predicted and observed σ_t , where the VF(d) model appears to give the closest prediction of all, with a slight disagreement (underprediction of about 12%) on the GOM2 case where it still seems within the observed scatter in GOM1 and GOM2. The normalized maximum displacement (bottom-left figure in Fig. 3.10) shows a similar result as seen for the surge component case (in Fig. 3.4). This is because the other two contributing components (pitch, and wave-frequency) generally show good agreement in the normalized maximum displacement comparisons (see Figs. 3.1 and 3.4). Finally, the bottom-right plot in Fig. 3.10 reports the maximum horizontal displacement of the total response. We find that the DF/WDD model predicts smaller maximum response levels than the DF model, and inclusion of viscous effects makes the agreement better.

A qualitative comparison of the predicted and measured combined time histories is shown in Figs. 3.11, 3.12, and 3.13 for the three seastates, respectively. We will first look at the GOM1 test in Fig. 3.11. As noted previously (in Fig. 2.4), the measured displacement shows a transition in the response around 1500 seconds (from visual

inspection). The prediction models also show a similar transition: the DF and VF(u) models around 1800 seconds, and the VF(d) also around 1500 seconds. Also around 500 seconds, the general nature of the prediction differs among the three models. Here again, the VF(d) model seems to better compare with the measurements. Similarly, for the GOM2 test in Fig. 3.12, the predicted amplitudes and phases generally follow the measured results in the top plot. The prediction models appear to have different frequency-component contribution around 2500 seconds, and of these the VF(d) model seems to be closest to measurements. Finally, for the NS case in Fig. 3.13, the prediction models predict similar displacements after about 2500 seconds. From about 1000 to 2500 seconds, we find absence of the low-cycle or surge frequency components when compared to the measured result. This was also seen in Fig. 3.5 where the predicted surge component is very small compared to the observed component. For the VF(u) model, it seems that in the same time range (100 to 2500 seconds) even the pitch component is underpredicted, and the total predicted displacement is predominantly first-order.

The prediction models, in general, seem to predict the GOM1 and GOM2 test results better than in the NS case. Recall the difficulty in calibrating pitch damping ratios for the NS case (that turned out to be almost zero).

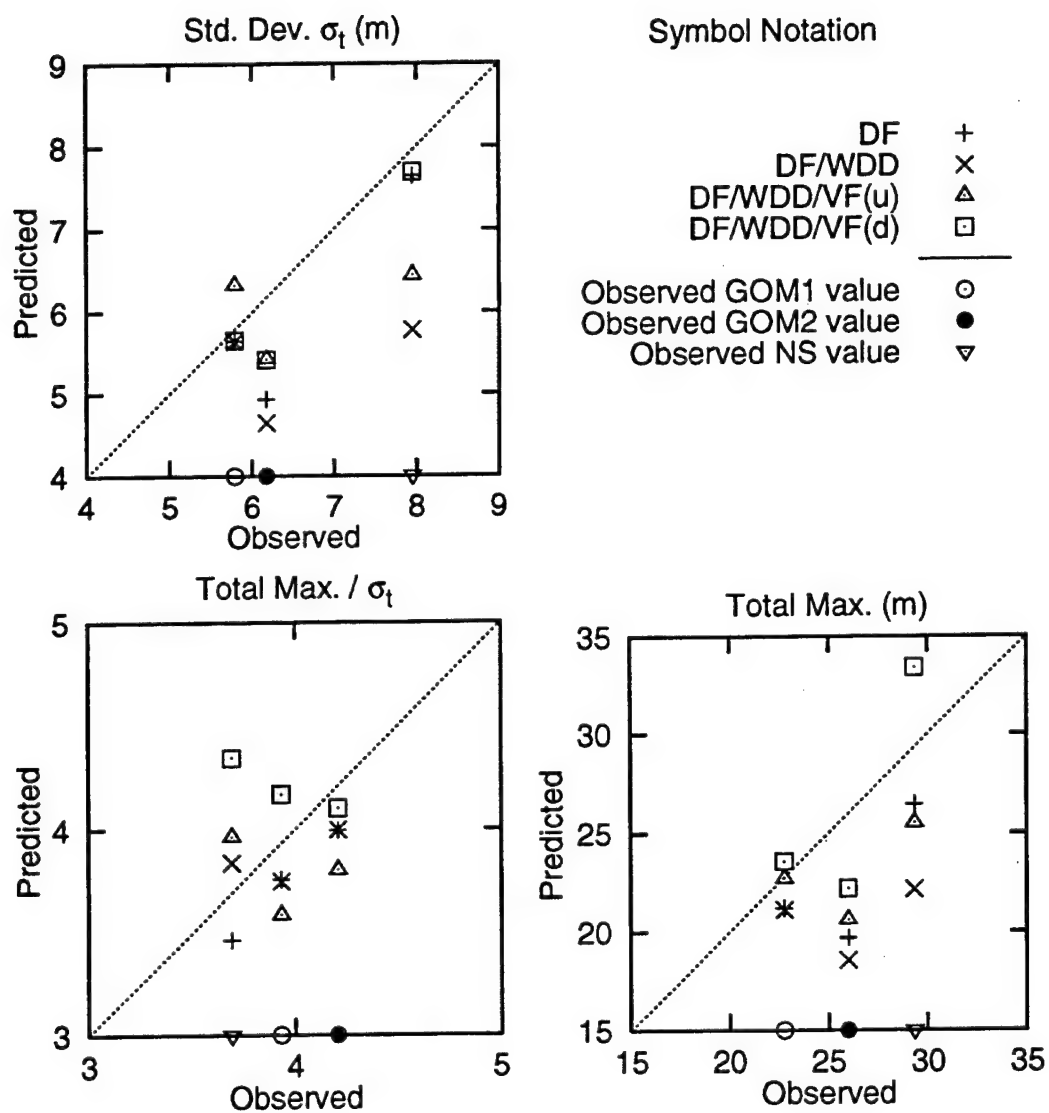


Figure 3.10: Comparison of standard deviation and maximum of combined response: prediction vs. measurement

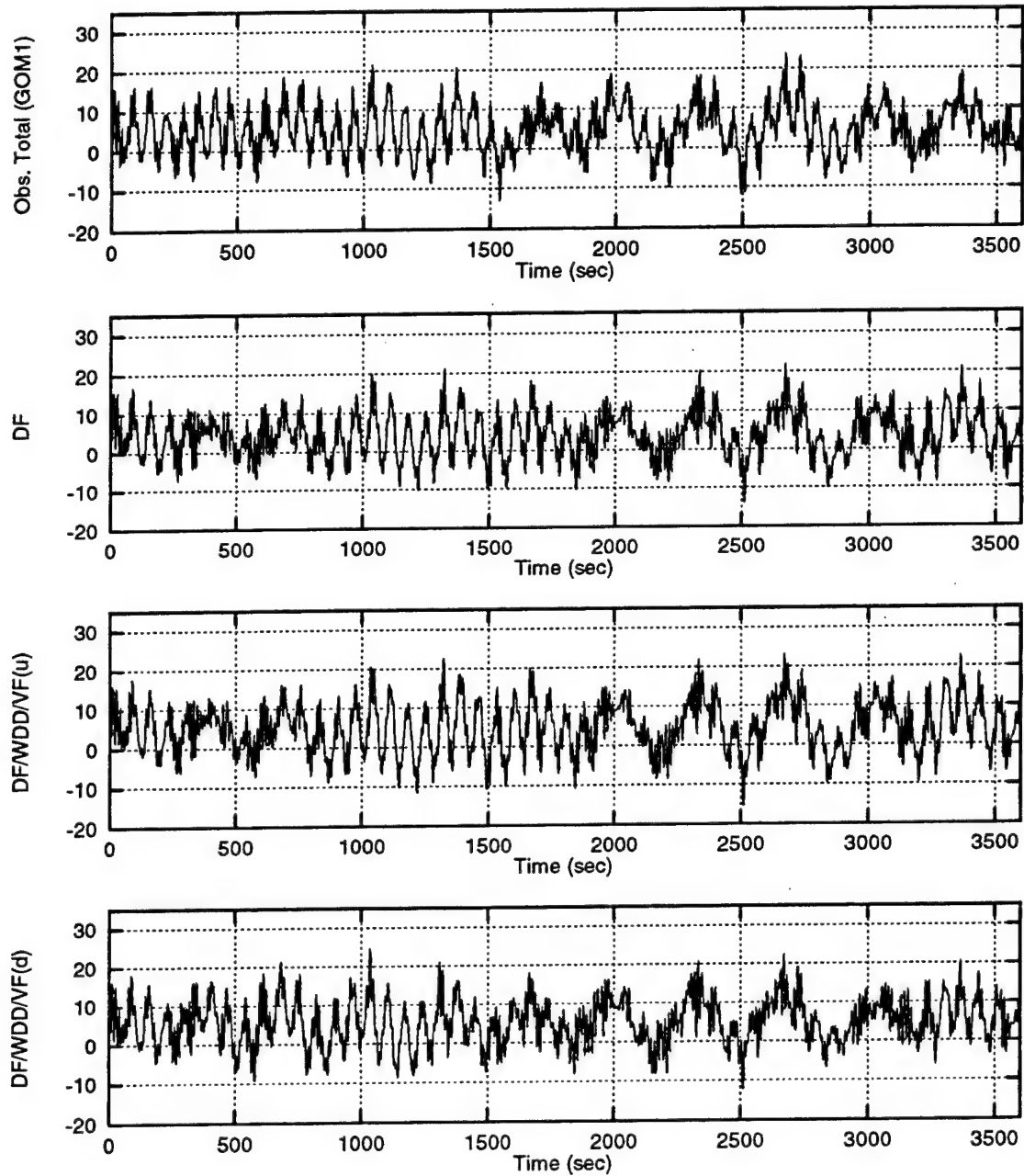


Figure 3.11: Combined (total) surge response time history for GOM1: prediction vs. measurement

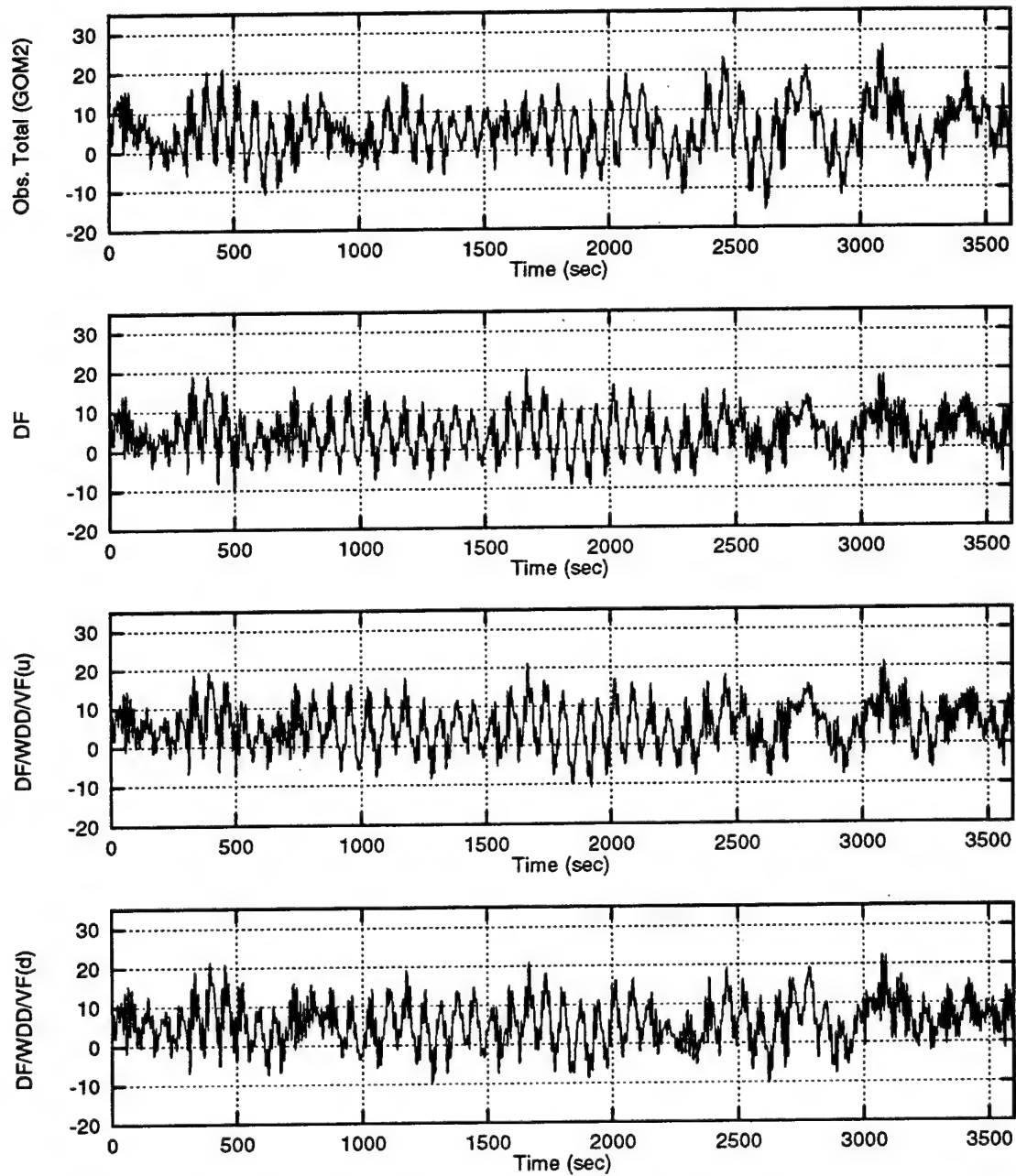


Figure 3.12: Combined (total) surge response time history for GOM2: prediction vs. measurement

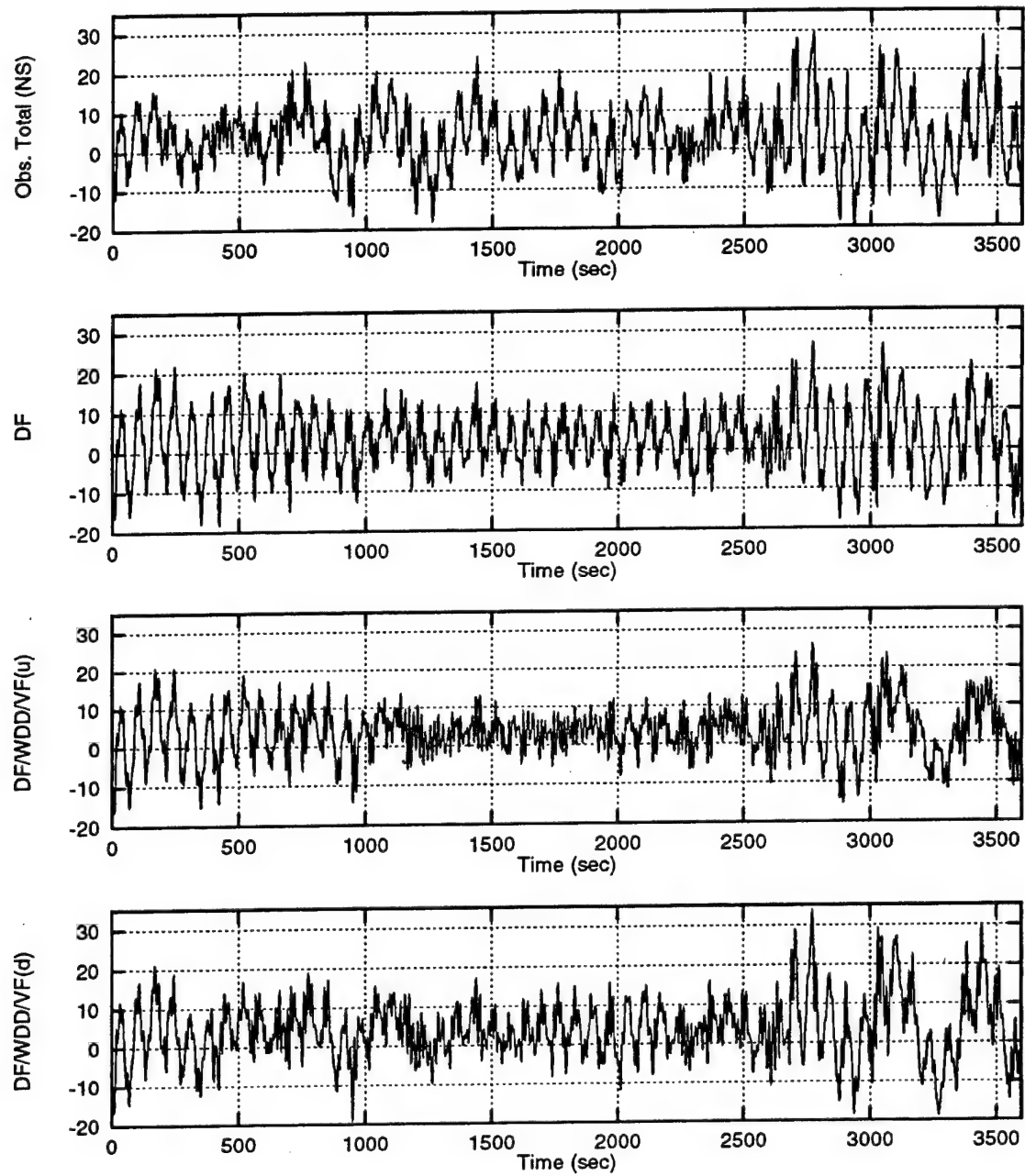


Figure 3.13: Combined (total) surge response time history for NS: prediction vs. measurement

Chapter 4

Conclusion and Future Work

4.1 Conclusion

In order to predict the global response of a spar platform, we used different hydrodynamic force models and applied it to a linear rigid-body model of the spar. Such models have been applied earlier to other large-volume floating structures. Existing studies on the spar, however, do not appear to systematically compare model predictions in the case of random sea measurements.

Geometry considerations led to the development of the rigid-body structural model and the incident forces were modeled as second-order diffraction forces. We incrementally added other hydrodynamic effects, for example: the wave drift damping, and viscous forces on the spar (from disturbed or undisturbed waves) in order to better match model predictions to data. For the damping characteristics (over and above the added/diffraction damping and wave drift damping) of the spar, we calibrated the damping ratios in each of the two contributing modes (surge and pitch) so that the predicted spectral bandwidth matched observed results.

The limited number of response cycles (in surge) and the apparent "mode-swapping" in the measured horizontal displacements posed practical difficulties in calibrating the prediction models to the measured results. We applied measured initial conditions in an effort to better predict such transient characteristics.

The prediction models generally appear to give good agreement with the measured results. The comparisons were based on the moments (mean, standard deviation and maximum displacement) of the predicted and measured time histories, as well as on direct comparison of the time histories itself. Such comparisons were made for the total displacement histories and its filtered components (surge, pitch, and wave-frequency) across the three random sea measurements (reflecting severe storm conditions) in the wave tank.

We surveyed four prediction models: (1) nonlinear diffraction forces only, (2) diffraction force plus wave drift damping effect, (3) model 2 plus additional viscous forces due to undisturbed waves, and (4) model 2 plus viscous forces from disturbed waves. The diffraction force model seemed to underpredict the observed mean offset, inclusion of viscous effects then better predicted the mean offset. The four models generally give good agreement with observed results and even appear to predict the apparent mode-swapping seen in the observations.

4.2 Future Work

The first proposal is to perform additional investigations in an effort to further improve the agreement between the predicted and measured results. We could, for example, investigate half-hour measurements instead of the hourly measurement in

an attempt to identify effects of nonstationarity on predicted response. Another interesting study would be to quantify the mode-swapping effects seen in the measured histories using a moving window. We could study a ratio of the rms surge to pitch response across these windows and develop a strategy for identify the occurrence of mode-swapping ranges in the time history. We could similar scheme to the predicted history as well and the compare it to measured results.

In the model formulations, we suggest investigating other schemes to calibrate the damping ratios in the four prediction models. For example, we could tune the damping estimates to match the rms of the measured response, instead of the spectral bandwidth as used in this study. The model accuracy can then be gauged by comparing the predicted and measured spectral bandwidths. The methods studied in this dissertation can be extended to other responses, for example, the heave response of the spar in random waves to design the airgap of the spar.

Given successful comparison of predicted results to measurement, the model can be applied, for example, to perform a fatigue or ultimate strength analysis of the spar. We could use these to develop load and resistance design factors for the limit states considered.

Bibliography

- [1] Vanmarcke E. Properties of spectral moments with applications to random vibration. *Journal of Engineering Mechanics*, 98, 1972.
- [2] O. M. Faltinsen. *Sea Loads on Ships and Offshore Structures*. Cambridge University Press, 1990.
- [3] A. K. Jha. Nonlinear random ocean waves: Prediction and comparison with data. Technical Report RMS-24, Civil Engr. Dept., Stanford University, Reliability of Marine Structures, 1997.
- [4] A. K. Jha. *Nonlinear stochastic models for loads and responses of offshore structures and vessels*. PhD thesis, Stanford University, 1997.
- [5] A. K. Jha, P. R. de Jong, and S. R. Winterstein. Motions of a spar buoy in random seas: Comparing predictions and model test results. In *Proceedings, Behavior of Offshore Structures BOSS-97*. Delft Univ., 1997. To be presented.
- [6] A. K. Jha and S. R. Winterstein. Simulation and identification of second-order random waves. Technical Report RMS-22, Reliability of Marine Structures Program, Stanford University, Dept. of Civil Engineering, 1996.

- [7] A.K. Jha. QTF surface spline interpolation: A pre-processor to TFPOP. Technical report, Reliability of Marine Structures, 1996. In TFPOP report RMS-18.
- [8] M.H. Kim and D.K.P. Yue. The complete second-order diffraction solution for an axisymmetric body. Part 1: Monochromatic incident waves. *Journal of Fluid Mechanics*, 200:235-264, 1989.
- [9] M.P. Kim and D.K.P. Yue. Sum- and difference-frequency wave loads on a body in unidirectional gaussian seas. *Journal of Ship Research*, 35(2):127-140, 1991.
- [10] Massachusetts Institute of Technology, Department of Ocean Engineering, Cambridge. *SWIM: Users Manual*.
- [11] B. B. Mekha, D. C. Weggel, C. P. Johnson, and J. M. Roesset. Effects of second order diffraction forces on the global response of spars. In *ISOPE*, 1996. To appear.
- [12] B.B. Mekha, C.P. Johnson, and J.M. Roesset. Nonlinear response of a spar in deep water: Different hydrodynamic and structural models. In *5th International Offshore and Polar Engineering Conference (ISOPE)*, volume III, pages 462-469, The Hague, The Netherlands, 1995.
- [13] J.N. Newman. Second order, slowly varying forces on vessels in irregular waves. In Bishop R.D. and Price W.G., editors, *Proc. Int. Symp. Dynamics of Marine Vehicles and Structures in waves*, pages 182-186. Mechanical Engineering Publications, 1974.
- [14] OTRC. Spar model test: Joint industry project - final report, volume I. Technical report, Offshore Technology Research Center, 1995.

- [15] Z. Ran, M.-H. Kim, J.M. Niedzwecki, and R.P. Johnson. Responses of a spar platform in random waves and current. In *5th International Offshore and Polar Engineering Conference (ISOPE)*, volume III, pages 363–371, The Hague, The Netherlands, 1995.
- [16] SWIM 2.0. *SWIM: Slow Wave-Induced Motions– User’s Manual*. Dept. of Ocean Engineering, M.I.T., 1995.
- [17] T. C. Ude, S. Kumar, and S. R. Winterstein. Stochastic response analysis of floating structures under wind, current, and second-order wave loads. Technical Report RMS-18, Reliability of Marine Structures, Civil Engineering Department, Stanford University, 1996.
- [18] T. C. Ude and S. R. Winterstein. Calibration of models for slow drift motions using statistical moments of observed data. In *6th International Offshore and Polar Engineering Conference ISOPE*, 1996.
- [19] J.K. Vandiver and A.B. Dunwoody. A mathematical basis for the random decrement vibration signature analysis technique. *ASME Journal of Mechanical Design*, 1981. Paper No. 81-DET-13.
- [20] WAMIT 4.0. *WAMIT: A Radiation-Diffraction Panel Program for Wave-Body Interactions–User’s Manual*. Dept. of Ocean Engineering, M.I.T., 1995.
- [21] D.C. Weggel and J.M. Roesset. Second-order dynamic response of a large spar platform: Numerical predictions versus experimental results. In *15th International Conference on Offshore Mechanics and Arctic Engineering (OMAE)*, Florence, Italy, 1996. ASME.

- [22] J.D. Wheeler. Method for calculating forces produced by irregular waves. *Journal of Petroleum Technology*, pages 359–367, March 1970.

Appendix A

Methodology of First-order Wave Identification

The details of this methodology and some application of this can also be found in Reference [3].

The idea here is to identify the implied first-order history $\eta_1(t)$ (of an observed history $\eta_{\text{obs}}(t)$) which, when run through the second-order predictor, yields an incident wave that agrees with $\eta_{\text{obs}}(t)$. The reader is referred to [3, 6] for details on the algorithm and the wave identification studies.

In the first-order wave process $\eta_1(t)$ written as a Fourier sum of N frequencies,

$$\eta_1(t) = \sum_{k=1}^{N/2} A_k \cos(\omega_k t + \theta_k) = \sum_{k=1}^N X_k e^{i\omega_k t} \quad (\text{A.1})$$

we need to identify only the lower half X_k components, since the upper half values are complex conjugates of the lower half. Let us denote $X_k = U_k + iV_k$, where U_k , V_k are the real and imaginary parts of the complex Fourier component X_k , respectively.

The predicted second-order wave process as evaluated from the QTFs is

$$\Delta\eta_2(t) = 2\text{Re} \sum_{m=1}^{N/2} \sum_{n=1}^{N/2} X_m X_n H_{mn}^+ e^{i(\omega_m + \omega_n)t} + X_m X_n^* H_{mn}^- e^{i(\omega_m - \omega_n)t} \quad (\text{A.2})$$

This may be rewritten in the form of a Fourier sum as

$$\Delta\eta_2(t) = \sum_{k=1}^N Y_k e^{i\omega_k t} \quad (\text{A.3})$$

where $Y_k = Y_k^+ + Y_k^-$ are the combined sum and difference frequency components. Here again, Y_k possesses conjugate symmetry so that only the lower half contains unique information. Y_k^+ can be shown to be

$$\begin{aligned} Y_k^+ &= \sum_{m+n,k} X_m X_n H_{mn}^+ \\ &= \sum_{m+n,k} [(U_m U_n - V_m V_n) + i(V_m U_n + U_m V_n)] H_{mn}^+ \end{aligned} \quad (\text{A.4})$$

where the summation symbol indicates a double summation

$$\sum_{m+n,k} = \sum_{m=1}^{N/2} \sum_{n=1}^{N/2} \quad \text{such that } \omega_m + \omega_n = \omega_k \quad (\text{A.5})$$

and

$$\begin{aligned} Y_k^- &= \sum_{m-n,k} X_m X_n^* H_{mn}^- \\ &= \sum_{m-n,k} [(U_m U_n + V_m V_n) + i(V_m U_n - U_m V_n)] H_{mn}^- \end{aligned} \quad (\text{A.6})$$

where

$$\sum_{m-n,k} = \sum_{m=1}^{N/2} \sum_{n=1}^{N/2} \quad \text{such that } |\omega_m - \omega_n| = \omega_k \quad (\text{A.7})$$

The combined predicted wave process is

$$\eta_{\text{pred}}(t) = \eta_1(t) + \Delta\eta_2(t) \quad (\text{A.8})$$

The identification scheme strives to simultaneously match $\eta_{\text{pred}}(t)$ to the observed wave history $\eta_{\text{obs}}(t)$ at every value of t . Alternatively, we can perform the identification in the frequency domain and strive to simultaneously match the predicted Fourier components to the observed Fourier components at all frequencies.

$\eta_{\text{obs}}(t)$ can be represented in the frequency domain as

$$\eta_{\text{obs}}(t) = \sum_{k=1}^N Z_k e^{i\omega_k t} \quad (\text{A.9})$$

where Z_k 's also possess conjugate symmetry. If the first-order components are identified exactly, from Eqn.s A.1, A.3 and A.9 we will have

$$Z_k = X_k + Y_k \quad ; \quad \text{for all } k = 1 \dots N/2 \quad (\text{A.10})$$

Note that the upper half values can be obtained from conjugate symmetry of the lower half values. In the Newton-Raphson identification scheme we will try to simultaneously minimize $X_k + Y_k - Z_k$; for $k = 1 \dots N/2$ to achieve convergence. Now, this scheme requires a Jacobian of $X_k + Y_k - Z_k$ with respect to the unknowns X_k —such a complex differentiation will lead to numerical discontinuities so we will minimize an equivalent real function $\sqrt{\sum_1^N f_k^2 / N}$ instead, where for $k = 1 \dots N/2$

$$\begin{aligned} f_k &= \text{Re}(X_k + Y_k - Z_k) \\ f_{k+N/2} &= \text{Im}(X_k + Y_k - Z_k) \end{aligned} \quad (\text{A.11})$$

The identification of the lower half X_k values requires a simultaneous solution of the nonlinear equations in A.11 such that $f_k \rightarrow 0$ for all $k = 1 \dots N$, or alternately $\sqrt{\sum_1^N f_k^2}/N \rightarrow 0$. We will formulate the Newton-Raphson scheme in vector form as

$$\mathbf{f} = \left[\frac{\text{Re}\mathbf{X}}{\text{Im}\mathbf{X}} \right] + \left[\frac{\text{Re}\mathbf{Y}}{\text{Im}\mathbf{Y}} \right] - \left[\frac{\text{Re}\mathbf{Z}}{\text{Im}\mathbf{Z}} \right] \quad (\text{A.12})$$

where bold face letters denote vectors, and vectors $\mathbf{X}, \mathbf{Y}, \mathbf{Z}$ contain the complex Fourier components X_k, Y_k, Z_k , $k = 1 \dots N/2$, respectively. Here, $\left[\frac{\text{Re}\mathbf{X}}{\text{Im}\mathbf{X}} \right]$ is a vector containing the real part of \mathbf{X} in the upper half and the imaginary part of \mathbf{X} in the lower half.

Let us denote

$$\begin{aligned} \mathbf{A} &= \left[\frac{\text{Re}\mathbf{X}}{\text{Im}\mathbf{X}} \right] = \left[\begin{array}{c} \mathbf{U} \\ \mathbf{V} \end{array} \right] \\ \mathbf{B} &= \left[\frac{\text{Re}\mathbf{Y}}{\text{Im}\mathbf{Y}} \right] \\ \mathbf{C} &= \left[\frac{\text{Re}\mathbf{Z}}{\text{Im}\mathbf{Z}} \right] \end{aligned} \quad (\text{A.13})$$

Note that the vector \mathbf{A} , of length N , is constructed such that lower half values are the real parts of X_k ; $k = 1 \dots N/2$ and the upper half is the imaginary part of X_k ; $k = 1 \dots N/2$. Similarly, \mathbf{B} and \mathbf{C} , each of length N , contain real and imaginary parts of the lower half of the second-order correction and the observed Fourier components, respectively. The elements of \mathbf{A} and \mathbf{B} are denoted by a_l and b_k , respectively, where $l, k = 1 \dots N$. The objective function in vector notation now is

$$\mathbf{f}(\mathbf{A}) = \mathbf{A} + \mathbf{B} - \mathbf{C} \quad (\text{A.14})$$

A first-order Taylor approximation of $\mathbf{f}(\mathbf{A})$ about a given $\mathbf{A}^{(0)}$ is

$$\mathbf{f}(\mathbf{A}) = \mathbf{f}(\mathbf{A}^{(0)}) + [\mathbf{J}](\mathbf{A} - \mathbf{A}^{(0)}) \quad (\text{A.15})$$

where $[\mathbf{J}]$ is a $N \times N$ Jacobian matrix denoting the derivatives of the elements f_k in vector $\mathbf{f}(\mathbf{A})$ with respect to each of the unknowns a_l in \mathbf{A} where $k, l = 1 \dots N$. The Newton-Raphson scheme at iteration $p + 1$ is then formulated as

$$\mathbf{A}^{(p+1)} = \mathbf{A}^{(p)} + \mathbf{h} \quad (\text{A.16})$$

where \mathbf{h} , a vector of length N , is found from a Cholesky decomposition followed by a back-substitution scheme from

$$[\mathbf{J}]\mathbf{h} = -\mathbf{f}(\mathbf{A}^{(p)}) \quad (\text{A.17})$$

It can be easily shown from Eqn. A.14 that the entries $J_{k,l}$ of the matrix $[\mathbf{J}]$ are

$$J_{k,l} = \frac{\partial f_k}{\partial a_l} = \delta_{kl} + \frac{\partial b_k}{\partial a_l} \quad (\text{A.18})$$

where $\partial b_k / \partial a_l$ indicates the partial derivative of b_k with respect to a_l , and

$$\delta_{kl} = \begin{cases} 1 & \text{if } k = l \\ 0 & \text{otherwise} \end{cases} \quad (\text{A.19})$$

To find $\partial b_k / \partial a_l$, recall from notation in A.13

$$b_k = \text{Re}Y_k \quad \text{and} \quad b_{k+N/2} = \text{Im}Y_k \quad \text{for } k = 1 \dots N/2$$

$$a_l = \text{Im}X_l = U_l \quad \text{and} \quad a_{l+N/2} = \text{Im}X_l = V_l \quad \text{for } l = 1 \dots N/2$$

so that from Eqn.s A.4 and A.6 we have

$$\begin{aligned} \frac{\partial \text{Re}Y_k}{\partial U_l} &= \sum_{m+n,k} (U_n \delta_{ml} + U_m \delta_{nl}) H_{mn}^+ + \sum_{m-n,k} (U_n \delta_{ml} + U_m \delta_{nl}) H_{mn}^- \\ \frac{\partial \text{Re}Y_k}{\partial V_l} &= \sum_{m+n,k} -(V_n \delta_{ml} + V_m \delta_{nl}) H_{mn}^+ + \sum_{m-n,k} (V_n \delta_{ml} + V_m \delta_{nl}) H_{mn}^- \quad (\text{A.20}) \\ \frac{\partial \text{Im}Y_k}{\partial U_l} &= \sum_{m+n,k} (V_m \delta_{nl} + V_n \delta_{ml}) H_{mn}^+ + \sum_{m-n,k} (V_m \delta_{nl} - V_n \delta_{ml}) H_{mn}^- \\ \frac{\partial \text{Im}Y_k}{\partial V_l} &= \sum_{m+n,k} (U_n \delta_{ml} + U_m \delta_{nl}) H_{mn}^+ + \sum_{m-n,k} (U_n \delta_{ml} - U_m \delta_{nl}) H_{mn}^- \end{aligned}$$

Schematically,

$$[J] = [I] + \left[\begin{array}{c|c} \frac{\partial \text{Re}Y_k}{\partial U_l} & \frac{\partial \text{Re}Y_k}{\partial V_l} \\ \hline \frac{\partial \text{Im}Y_k}{\partial U_l} & \frac{\partial \text{Im}Y_k}{\partial V_l} \end{array} \right] \quad (\text{A.21})$$

where $[I]$ is the identity matrix.

Appendix B

FITQTF: QTF Surface Spline Interpolation—A Pre-processor to TFPOP

B.1 Introduction

A need to have better interpolation schemes for QTFs in second-order analysis using TFPOP [17] motivated the development of this tool. The analysis required to obtain QTF values is usually an expensive process, as a result the values are estimated only for a sparse number of frequency pairs. TFPOP provides options for a few interpolation schemes (see [17]), that are based on weighted linear interpolation of QTF values within a specified radius. This tool supplements the available interpolation schemes in TFPOP and provides for a flexible means of interpolating a sparse QTF data set into a fine mesh for direct input to TFPOP. The salient features of this tool are:

- The input QTF data is in WAMIT [20] format, this is also the format in which TFPOP reads in the QTFs. The output interpolated QTF is also in a format that TFPOP can read directly.
- The input QTF can be a sparse data set on a regular or irregular grid of frequency (period) pairs. The data set need not be any order. Due to symmetry conditions, the input QTF should only be provided on either the upper or the lower triangle about the principal diagonal ($\omega_i = \omega_j$) of the frequency axis.
- The interpolation is based on a flexible scheme of surface-fitting. FITQTF allows for surface-spline fits of various orders in both frequency directions.
- The interpolation can be based on the axes being any one of frequency (Hz), wave period (seconds), wavelength (meters), or wave number (per meter).

B.2 Interpolation Options

The input QTF is interpolated by fitting spline surfaces of different orders, k_x and k_y (specified by the user), in the two directions x and y . FITQTF can fit splines of orders ranging from 1 through 5 in each direction. Different orders of splines can be chosen in the two directions. The data can also be rotated by 45 degrees in the frequency plane and then interpolated. This rotated interpolation offers a benefit of fitting along the principal diagonal, for example, without using any information from the off-diagonal terms. The user can also specify the x and y coordinate axes used in interpolation to be one of: frequency (Hz), wave period (seconds), wavelength (meters), or wave number (per meter).

Table B.1: Description of error messages from FITQTF

	Description
ier	Unless the routine detects an error, ier contains a non-positive value on exit
ier=0	Normal return. the spline returned has a residual sum of squares fp such that $\text{abs}(fp-s)/s \leq \text{tol}$ with tol a relative tolerance set to 0.001 by the program
ier=-1	Normal return. the spline returned is an interpolating spline (fp=0)
ier=-2	Normal return. the spline returned is the weighted least- squares polynomial of degrees kx and ky. in this extreme case fp gives the upper bound for the smoothing factor s

FITQTF requires as input a parameter s that governs the level of smoothing desired in fitting the surface data. A very large value of s will result in a least-squares fit to the surface, while, in theory, a value $s = 0$ will result in an interpolating spline. However, such an interpolating spline may not always be possible owing to possible theoretical (refer to the subroutine comments regarding more details on s and corresponding error messages). Public domain subroutines (`surfit` and `bispev`) are used to fit a surface to the QTF data and the resulting spline coefficients are used for interpolation. For a specified s value, the program tries to fit a surface and then estimates the sum of the residuals squared, and prints these out on standard error. Error flags are also printed to convey the success in fitting the data. The details of the interpretation of the error messages are in the comments of the subroutine `surfit`, and Table B.1 presents a list of "acceptable" error message values `ier`:

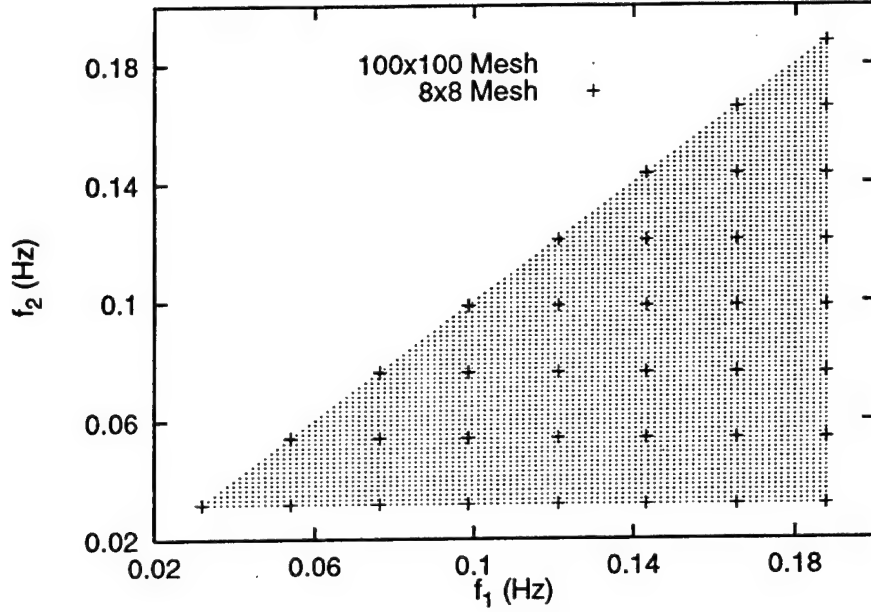


Figure B.1: Frequency grid points of the sparse and the finely meshed QTF values from SWIM

B.3 Verification Studies of FITQTF Interpolation

Some verification studies were done on the accuracy of interpolation from FITQTF for surge response analysis of the OTRC spar. For the spar modeled as a 1-DOF model in the surge direction, a diffraction analysis was performed on a fine mesh of difference frequency QTFs to generate the mean and standard deviation of the surge response. We also perform the same diffraction analysis, but now using various interpolated QTF schemes starting from a sparse QTF data set. The sparse QTF data set contains about 10 times fewer values than the fine mesh QTF as shown in Fig. B.1. Both the QTF data sets were generated using SWIM [16].

The diffraction analysis involved finding the mean, μ , and standard deviation, σ , of the surge response from direct statistics, and from an hourly prediction of the

response in a seastate characterized by $H_s = 14.1\text{m}$, $T_p = 13.8\text{s}$, $\gamma = 2.2$. Three models of the spar were analyzed, assuming the natural periods to be 330 sec, 100 sec, and 71 sec. Each of the three models were analyzed assuming two damping values of 2.4% and 5% in the surge direction. Thus, we have a total of six cases that were analyzed for μ and σ . "Exact" moments for these models were generated from the 100x100 finely meshed QTF. The moments were also generated using various interpolated QTFs starting from the 8x8 QTF and compared to the exact moments.

The different interpolation schemes adopted in this comparison study are:

- **realimag**: Using the TFPOP built-in interpolation on real and imaginary QTF values within a specified radius of 0.032 Hz.
- **11,0**: Using FITQTF to interpolate to a fine mesh by fitting linear splines in both directions without any rotation of the axes
- **11,45**: Using FITQTF to interpolate to a fine mesh by fitting linear splines in both directions after rotating the axes by 45 degrees
- **33,0**: Using FITQTF to interpolate to a fine mesh by fitting cubic splines in both directions without any rotation of the axes
- **33,45**: Using FITQTF to interpolate to a fine mesh by fitting cubic splines in both directions after rotating axes by 45 degrees

Figures B.2 and B.3 show μ and σ from direct statistics for the various interpolated QTFs versus the exact moments from the 100x100 QTF. Each vertical strip on these plots corresponds to a natural frequency, and along each vertical strip there are two sets of points corresponding to the two damping ratios used for each natural frequency. All the structures are analyzed assuming the same QTF, and are analyzed in the same

seastate so the mean surge does not depend on the natural period, as a result the mean ratio for an interpolation model does not change with natural period. Also, the damping ratio does not affect the mean, so we have two sets of mean for the two damping ratios lie on top of each other for a given natural frequency. It is seen from this plot that FITQTF substantially reduces the error in estimating the mean. The *realimag* interpolation yields about 8% smaller mean than the exact answer, and the FITQTF interpolations closer predictions.

Similarly, we see in Fig. B.3 that a bi-linear interpolation without any rotation is in error by a maximum of 20%, while the rest of the interpolation schemes give a significantly better fit to the exact answer across the three natural periods, and across the two damping ratios. The closest fit among the interpolation schemes shown, seems to be provided by the bi-cubic interpolation in both μ and σ .

Another set of comparison of the interpolated QTF moments to the exact moments are shown in Figs B.4 and B.5 for 1-hour prediction in the same seastate. Here again, we find similar observations as in the direct statistics comparison. The closest fit to the exact answer seems to be offered by the bi-cubic splines.

In conclusion, we find that FITQTF seems to offer a flexible, convenient and reliable means of interpolating the QTFs.

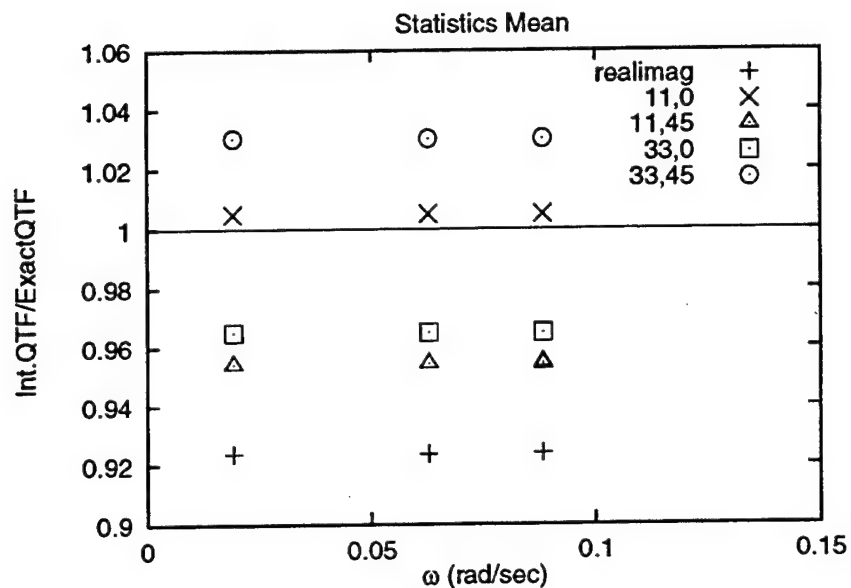


Figure B.2: Direct statistics mean for interpolated QTFs from sparse QTF vs. exact mean from finely meshed QTF (from diffraction analysis)

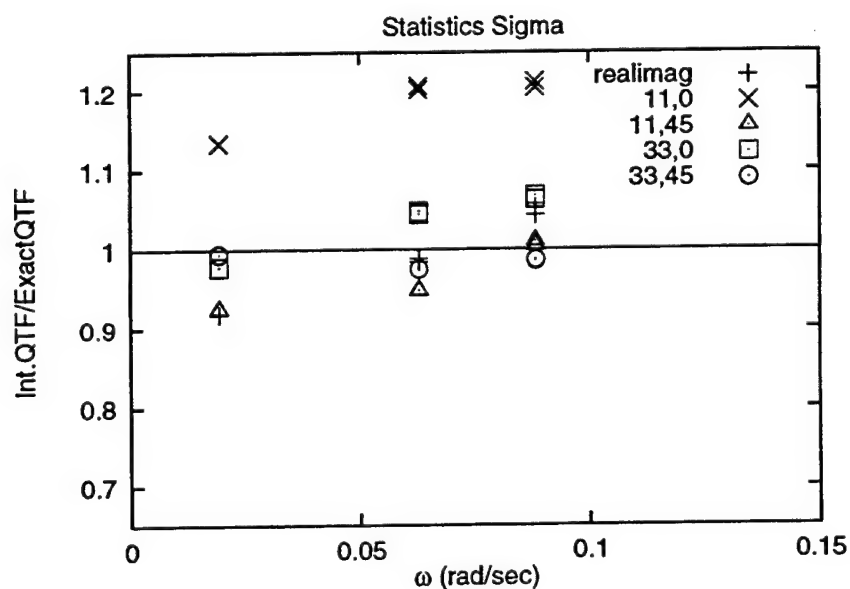


Figure B.3: Direct statistics standard deviation for interpolated QTFs from sparse QTF vs. exact mean from finely meshed QTF

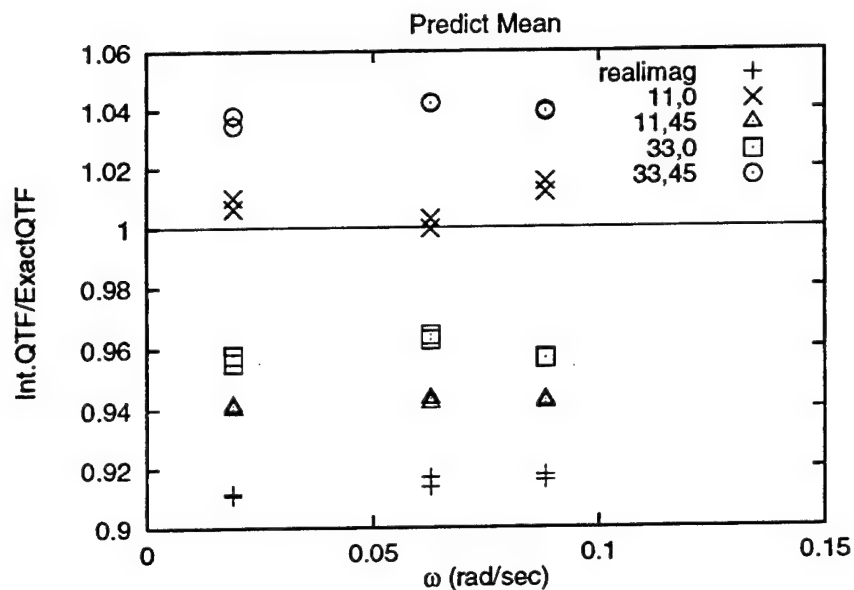


Figure B.4: 1-hour predicted mean for interpolated QTFs from sparse QTF vs. exact mean from finely meshed QTF

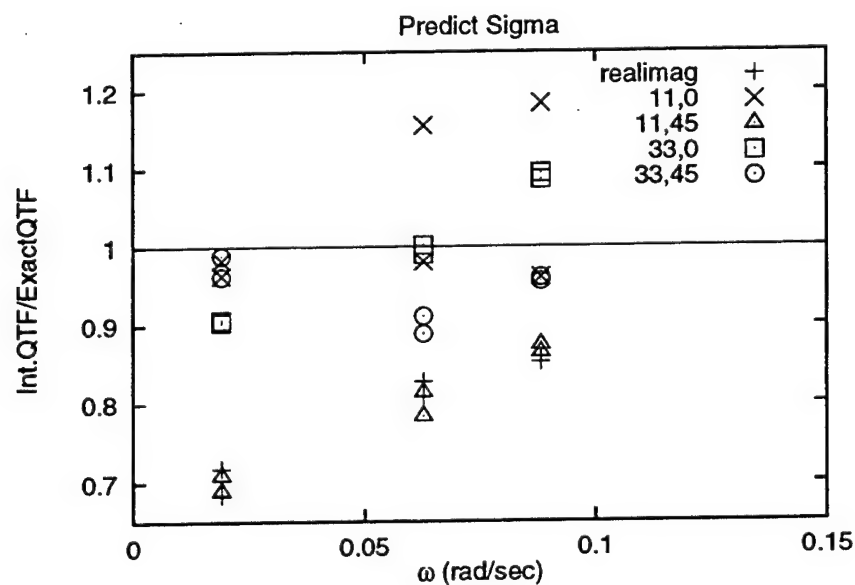


Figure B.5: 1-hour predicted standard deviation for interpolated QTFs from sparse QTF vs. exact mean from finely meshed QTF

Appendix C

Paper to be Presented at BOSS97

To be presented at *BOSS-97*, Delft Univ., July 1997.

MOTIONS OF A SPAR BUOY IN RANDOM SEAS: COMPARING PREDICTIONS AND MODEL TEST RESULTS

Alok K. Jha, P. R. de Jong, and Steven R. Winterstein

Civil Engineering Dept., Stanford University

ABSTRACT

This study compares the analytically predicted motions of a floating spar buoy platform with the results of wave tank experiments. Results studied include extreme conditions in both the Gulf of Mexico and the North Sea. Base-case predictions combine nonlinear diffraction loads and a linear, multi-degree-of-freedom model of the spar stiffness and damping characteristics. Refined models add the effect of wave-drift damping, and of viscous forces as well. Consistent choices of damping and wave input are considered in some detail. These successive model refinements are generally found to improve agreement with the model test results.

KEYWORDS

Nonlinear wave diffraction; offshore structures; random vibration; spar buoys, structural reliability; wave tank experiments.

INTRODUCTION

This study describes ongoing research into the statistical response behavior and reliability of a particular deep-water floating structure: a spar buoy. Typically, the spar buoy concept involves a deep-draft, large-diameter cylindrical floating structure, with slack or taut mooring (e.g., Glanville et al, 1991). This concept has recently gained increased interest within the offshore community. For example, Oryx has installed the first production spar (Neptune) in 1996, while Chevron is currently designing the first spar (Genesis) for both drilling and production. Concurrently, a particular spar buoy has been designated the "theme structure" of the NSF-sponsored Offshore Technology Research Center (OTRC), centered at Texas A&M University and at the University of Texas at Austin.

This study compares analytical predictions of spar surge motions with the results of model tests from the OTRC wave tank (OTRC, 1995). Comparisons are shown both for summary response statistics and for complete time histories. Consistent choices of damping and wave input are considered in some detail. Responses are filtered and compared for three distinct frequency ranges: a relatively high-frequency contribution due to first-order wave energy, a low-frequency contribution due to

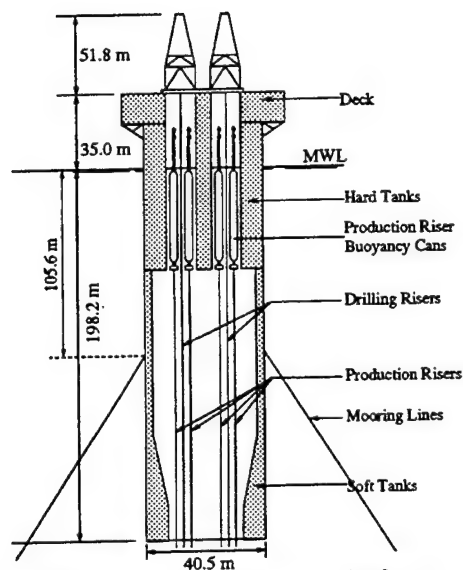


Figure 1: Elevation view of spar platform.

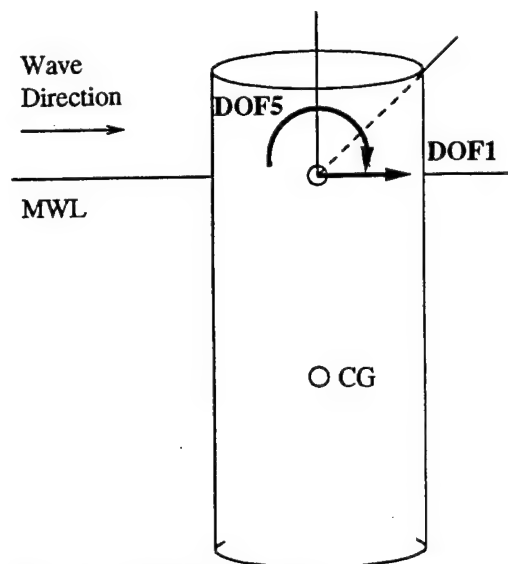


Figure 2: Degrees of freedom for spar.

pitch, and a still lower frequency contribution due to surge. Model tests are studied for extreme (100-year) conditions in both the Gulf of Mexico and the North Sea.

Results from analytical models are shown here over a range of increasing modelling detail. The base case includes nonlinear diffraction forces and a linear, multi-degree-of-freedom structural model. Refinements on this include the addition of wave drift damping, and then of viscous forces as well. These successively more detailed models are generally found to yield improved agreement with model test results. The analytical predictions also show the ability to capture another notable feature of the spar model tests; namely, the apparent "mode-swapping," between the spar response in pitch and surge modes, during the hour-long tests.

Spar Buoy Characteristics

Figure 1 shows the prototype dimensions of the spar buoy under study. Note its relatively deep draft ($H=198.2\text{m}$), particularly with respect to its diameter ($D=40.5\text{m}$). For prediction purposes the spar buoy hull is assumed rigid, and its mooring lines are modelled as a set of massless, linear springs. To predict the spar's motions in the along-wave direction, we adopt a 2DOF model that includes the surge motion $x_1(t)$ and pitch rotation $x_5(t)$ at the mean water level* (Figure 2). At an elevation z above this level, the corresponding along-wave displacement of the rigid spar is predicted simply as $x_1(t) + z \cdot x_5(t)$. In particular, we apply this result here with $z=54.8\text{m}$, to compare with video-recorded surge motions at this elevation during the wave tests (OTRC, 1995).

Mode Shapes and Periods

Assuming small deformations, the 2×2 stiffness and mass matrices can be constructed from geometrical considerations (Jha, 1997). This mass matrix includes added mass terms, reflecting first-order

*Note that we retain the common convention that numbers surge and pitch DOFs as "1" and "5" respectively, although no other DOFs are included here.

wave radiation effects. The resulting mode shapes and natural frequencies are

$$f_1 = \frac{1}{330} \text{ [Hz]}, \phi_1 = [1 \ 0]^T; \quad f_5 = \frac{1}{70} \text{ [Hz]}, \phi_5 = [100 \ 1]^T \quad (1)$$

These modal frequencies agree well with the natural periods, $T_1=330$ s and $T_5=67$ s, estimated from free-decay tests of the spar (OTRC, 1995). Note that this lower-frequency mode involves a pure translation, while the higher-frequency mode reflects a pure rotation about an axis located at depth 100m below the MWL. (Equivalently, Eq. 1 implies that a small rotation x_5 [rad] is accompanied by a translation of $x_1=100x_5$ [m] at the MWL.) These modes directly reflect the translational and rotational stiffnesses, respectively, of the spar's mooring system.

QUALITATIVE RESULTS AND CONSISTENT DAMPING ESTIMATES

We consider here the spar model tests that reflect extreme, roughly 100-year wave conditions. We also focus on tests that apply wave loads only, neglecting other tests that include simultaneous current and/or wind loads. This leaves us with three model tests, each lasting 1 hour (all time and length units here reflect prototype scale). Two of the three are separate realizations of 100-year Gulf of Mexico seastates, while the third models 100-year North Sea conditions. We refer here to these seastates as "GOM1", "GOM2", and "NS". (In OTRC internal reporting, these tests are respectively denoted "aran3", "aran4", and "aran5". To date, only "aran3" has received systematic study by OTRC investigators; e.g., Ran et al, 1996, Weggel and Roesset, 1996).

Wave Measurements and Characteristics

A reference, "undisturbed" wave elevation history has been measured during the OTRC tests by a probe located 125m (prototype scale) from the spar, in a direction perpendicular to the wave direction. The spectra of these waves are found to be relatively well-fit by JONSWAP spectral shapes with $\gamma=2$; the significant wave height and peak period values are estimated as $H_s=14.1$ m and $T_p=14.1$ s for the Gulf of Mexico seastates, and $H_s=14.8$ m and $T_p=16.1$ s for the North Sea test (Jha, 1997). Note however that our response predictions use the observed wave histories from the tests, and not the simulated input from a theoretical wave spectral model.

Response Measurements and Characteristics

Figure 3 shows the power spectrum of the spar displacement, measured at height $z=54.8$ m above MWL, during the GOM1 test. Note its two low-frequency modes, at around $f_1=1/330$ and $f_5=1/70$ Hz, reflecting motions induced by surge and pitch resonance. As Figure 3 shows, we use bandpass filters here to separate the observed surge component (0–.006 Hz), pitch component (.006–.03 Hz), and remaining wave frequency component (above .03 Hz). This gives rms response contributions of $\sigma_{\text{surge}}=3.4$ m, $\sigma_{\text{pitch}}=4.0$ m, and $\sigma_{\text{wave}}=2.5$ m. Thus a linear force model, which predicts energy only at the wave frequencies, would capture only a small portion of the response rms. It would also completely fail to predict the mean response, here found to be 4.9m. The other tests offer similar results. This shows the need for models of nonlinear forces—diffraction, drag or both—to explain not only the mean offset but also the amplitude of slow-drift oscillations for the spar. The effects of both nonlinear diffraction and drag loads are considered below.

Figure 4 shows the corresponding time history of the response during the GOM1 test. Both the total response and its filtered components are shown. Consistent with its power spectrum in Figure 3, the response indeed displays three distinct time scales. What Figure 3 fails to reveal, however, is that the relative contribution of the different frequency components does not remain constant over time. For the GOM1 test, the observed response changes qualitatively at around $t=1500$ s, when

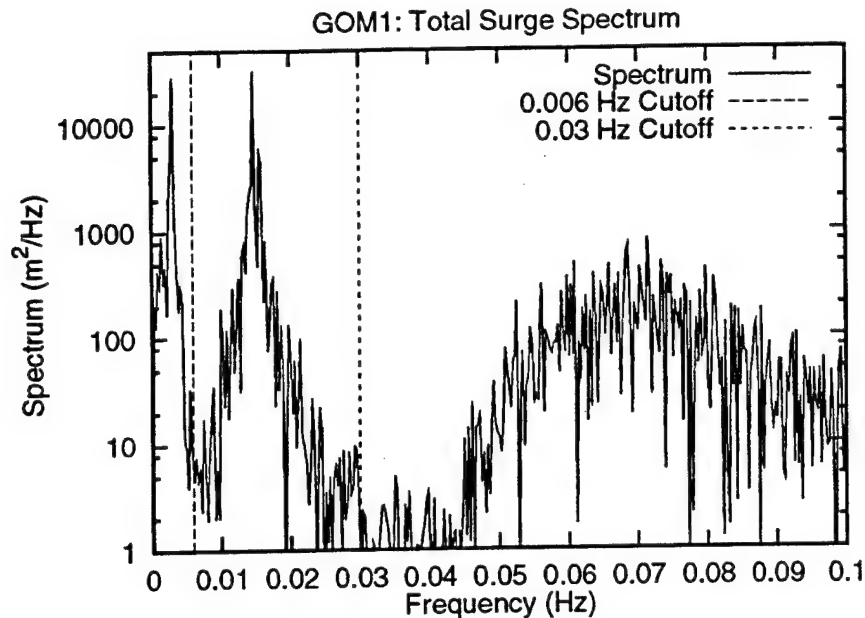


Figure 3: Spectrum of measured surge displacements at 54.8m elevation above MWL for GOM1 seastate

the surge component begins to contribute significantly. The other tests show somewhat similar shifts between the energy in surge and pitch modes—although this “mode swapping” is observed at different times, and for different durations, in different tests. The wave input histories show no such episodic nature. This reflects a further modelling challenge: can analytical models predict not only the correct average frequency content (e.g., the spectrum in Figure 3), but also time-domain behavior consistent with Figure 4? Clearly, this time-domain evolution of surge and pitch components depends directly on (1) their initial conditions at the beginning of the test recording and (2) the damping values assigned to these modes. We therefore discuss these issues, particularly damping estimation, in some detail.

Estimating Initial Conditions

In the experiments, spar motions were recorded after about 15 minutes (prototype scale), when the wave tank conditions were deemed to have achieved steady-state conditions. Thus, the assumption of at-rest initial conditions would corrupt our predictions, more so in the surge mode which contains relatively few cycles over the hour-long test. To avoid this, our predictions use initial conditions consistent with the tests; i.e., for each test we filter the observed motions to estimate surge and pitch components (e.g., Figure 4). The initial values/velocities of these components are then used to start our slow-drift motion predictions (Jha, 1997).

Estimating Surge and Pitch Damping

Because the tests include relatively few cycles of lightly damped motion, it is challenging to form precise damping estimates from them. We focus here on frequency-domain damping estimates, using response spectra from the various tests (e.g., Figure 3). One may, for example, select dampings

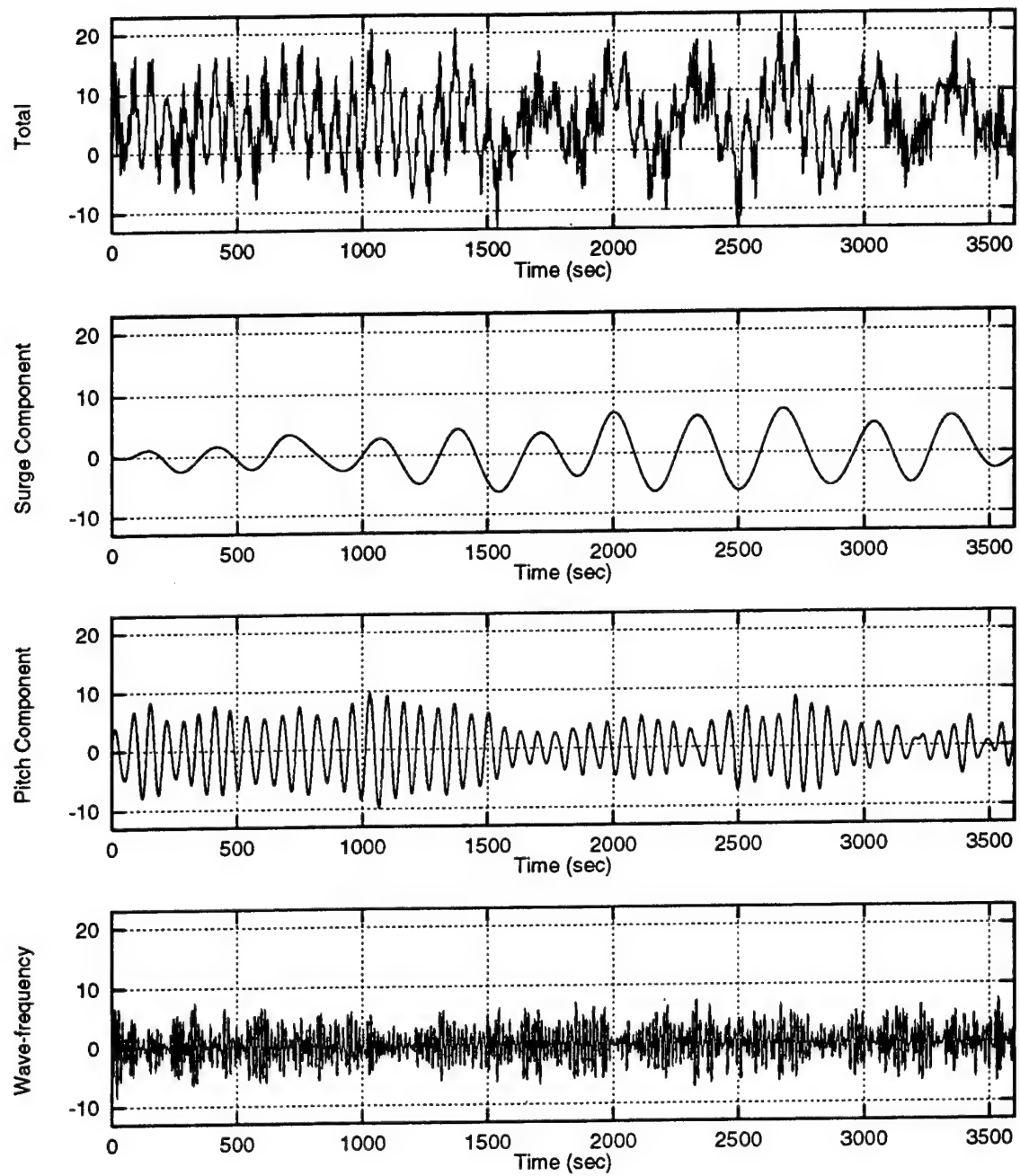


Figure 4: Total measured horizontal displacement and its filtered surge, pitch and wave-frequency components for GOM1 seastate

ζ_i so that our analytical model predicts the correct *area* under each of these observed spectral modes (i.e., the variances σ_{surge}^2 and σ_{pitch}^2). A danger in this approach is that it may mask a force modelling error (e.g., Ude, 1994). For example, if predicted forces are overestimated we may overestimate damping in an effort to compensate. Thus, we instead seek damping values to preserve the observed spectral *shape*—the rms values σ_{surge} and σ_{pitch} are reserved to test the model's adequacy. One such measure of spectral shape is the half-power bandwidth, at which the response spectrum decays to half its peak value. By setting this bandwidth to its approximate value from theory— $f_{HP} = \pm \zeta_i f_i$ to either side of the natural frequency f_i —one can estimate the damping ζ_i from an observed power spectrum. For example, if the spar buoy has damping $\zeta_1 = 0.05$ at the surge frequency $f_1 = 1/330$, we find $f_{HP} = 1/6600$ Hz. Unfortunately, from a $T = 1$ -hour history, our finest frequency resolution is $df = 1/T = 1/3600$ Hz—too coarse to resolve the half-power bandwidth, even if no frequency-averaging is applied to the observed spectrum.

We are therefore led to consider the average shape of the response spectrum across frequencies, as measured by the unitless bandwidth measure δ (Vanmarcke, 1972):

$$\delta = \sqrt{1 - \lambda_1^2 / (\lambda_0 \lambda_2)}; \quad \lambda_n = \int f^n S_x(f) df \quad (2)$$

Note that in general, any parameter of the form $\delta_n = [1 - \lambda_n^2 / (\lambda_0 \lambda_{2n})]^{1/2}$ could be used to reflect bandwidth: $\delta_n \rightarrow 0$ as the bandwidth narrows. Perhaps the most widely used is δ_2 , e.g. in modelling peaks of a Gaussian process. We use δ with $n=1$ here, as its lower spectral moments are less sensitive to high-frequency spectral content. We apply Eq. 2 twice, over the frequency ranges of surge (0–.006 Hz) and pitch (.006–.03 Hz) components, to find separate δ values that characterize their respective modal bandwidths.

For a 1DOF system under broad-band loads, δ can be related directly to the damping level (Vanmarcke, 1972; Ude and Winterstein, 1996). To form estimates consistent with our 2DOF model, however, we select damping ratios ζ_1 and ζ_5 so that our predicted response shows the same δ values, in both the surge and pitch frequency ranges, as found from the observed responses. This is an iterative process, which must be performed for each choice of (1) seastate and (2) predictive response model. We differentiate here between 2 seastates (GOM1 and GOM2 versus NS), and among 4 predictive models. These models are described below, together with the 2×4 values of modal dampings that result. In each case, a corresponding damping matrix C is inferred from the mass matrix and the matrix Φ of modal shapes: $C = M\Phi Q\Phi^{-1}$ in terms of $Q = \text{diag}(4\pi\zeta_i f_i)$.

Predictive Models of Forces and Damping

Our first, base-case model applies diffraction forces only (the “DF” model). Linear diffraction gives first-order transfer functions $F_1^{(1)}(\omega_k)$ and $F_5^{(1)}(\omega_k)$, the (complex) amplitude of surge force and pitch moment due to a unit-amplitude wave at frequency ω_k . A corresponding second-order diffraction analysis gives $F_1^{(2)}(\omega_k, \omega_j)$ and $F_5^{(2)}(\omega_k, \omega_j)$, the surge and pitch excitation amplitudes at the difference frequency $\omega_k - \omega_j$ due to pairs of incident waves at frequencies ω_k and ω_j (Kim and Yue, 1989; Kim and Yue, 1991). These subharmonic excitations drive the surge and pitch resonant motions, which dominate the spar response (e.g., Figure 3). Note that these diffraction forces assume as input not the undisturbed total wave elevation/potential but rather its first-order component. Here we use new methods (Winterstein and Jha, 1997) to identify the underlying first-order contribution to the observed undisturbed wave.

For this model, the damping matrix C gives the major source of damping. For example, Table 1 shows that this DF model requires the damping ratios $\zeta_1 = 4.5\%$ and $\zeta_5 = 1.6\%$ to match the spectral bandwidths estimated from the 2 GOM tests. In this (and other cases) the single NS test suggests rather lighter damping; indeed, an effectively zero value of pitch damping is not always able to give

Model	Description	GOM		NS	
		ζ_1	ζ_5	ζ_1	ζ_5
DF	Base-case model with diffraction forces	4.5	1.6	1.7	.001
DF/WDD	DF model plus wave-drift damping	3.3	0.6	.001	.001
DF/WDD/VF(u)	DF/WDD model plus viscous forces from undisturbed waves	4.0	0.5	2.5	.001
DF/WDD/VF(d)	DF/WDD model plus viscous forces from disturbed waves	6.5	.001	0.1	.001

Table 1: Description of 4 models, and consistent damping ratios ζ_1 and ζ_5 in surge and pitch.

as narrow a spectral bandwidth as observed. Note, however, that the NS test includes only a single hour, making narrow bandwidths more difficult to estimate than over the combined, two hours of GOM tests.

Our second model (DF/WDD) includes both diffraction forces and wave-drift damping. This damping force is proportional both to the structural velocity and to the square of the wave amplitude. The resulting nonlinear damping will tend to offset large slow drift forces, and perhaps reduce the extreme peaks of the surge response. We may expect that once wave drift damping is added, we require lower values of the additional modal damping ζ_i than in the DF model. Table 1 shows that this is indeed the case.

Finally, we also implement two models that include viscous drag forces as well as diffraction effects. These differ only in their choice of wave input: one uses the undisturbed waves, while the other uses the disturbed waves near the spar, inferred from its reported heave motions and the air-gap (structure-to-wave distance) measurements. Both models use the Morison's drag term with $C_D=0.6$, and Wheeler stretching (Wheeler, 1970) to integrate effects from the spar bottom to the free surface. They also both use the absolute fluid velocity; relative velocity effects are assumed reflected through damping terms.

NUMERICAL RESULTS

Wave-Frequency Response

We first compare the wave-frequency portions of the predicted and observed spar responses. These observed portions are found by applying a high-pass filter, with a low-frequency cutoff of .03 Hz., to the measured displacement histories. Figure 5 shows that these predictions fairly accurately predict not only the qualitative response behavior, but also its detailed cycle-by-cycle evolution in all three tests. This suggests that our models accurately reflect first-order wave forces, and the mass properties of the spar. (Because slow-drift forces and damping do not affect this wave-frequency response, all four of our models predict roughly the same histories in Figure 5. Thus, for clarity Figure 5 shows predictions only for the simplest (DF) model.)

Slow Drift Response

Figure 6 compares the predicted and observed moments of the slow-drift response. Results are shown for the rms values σ_1 and σ_5 , corresponding to frequency ranges (0-.006 Hz) and (.006-.03 Hz), and for the total mean offset (which cannot be split directly into surge and pitch contributions).

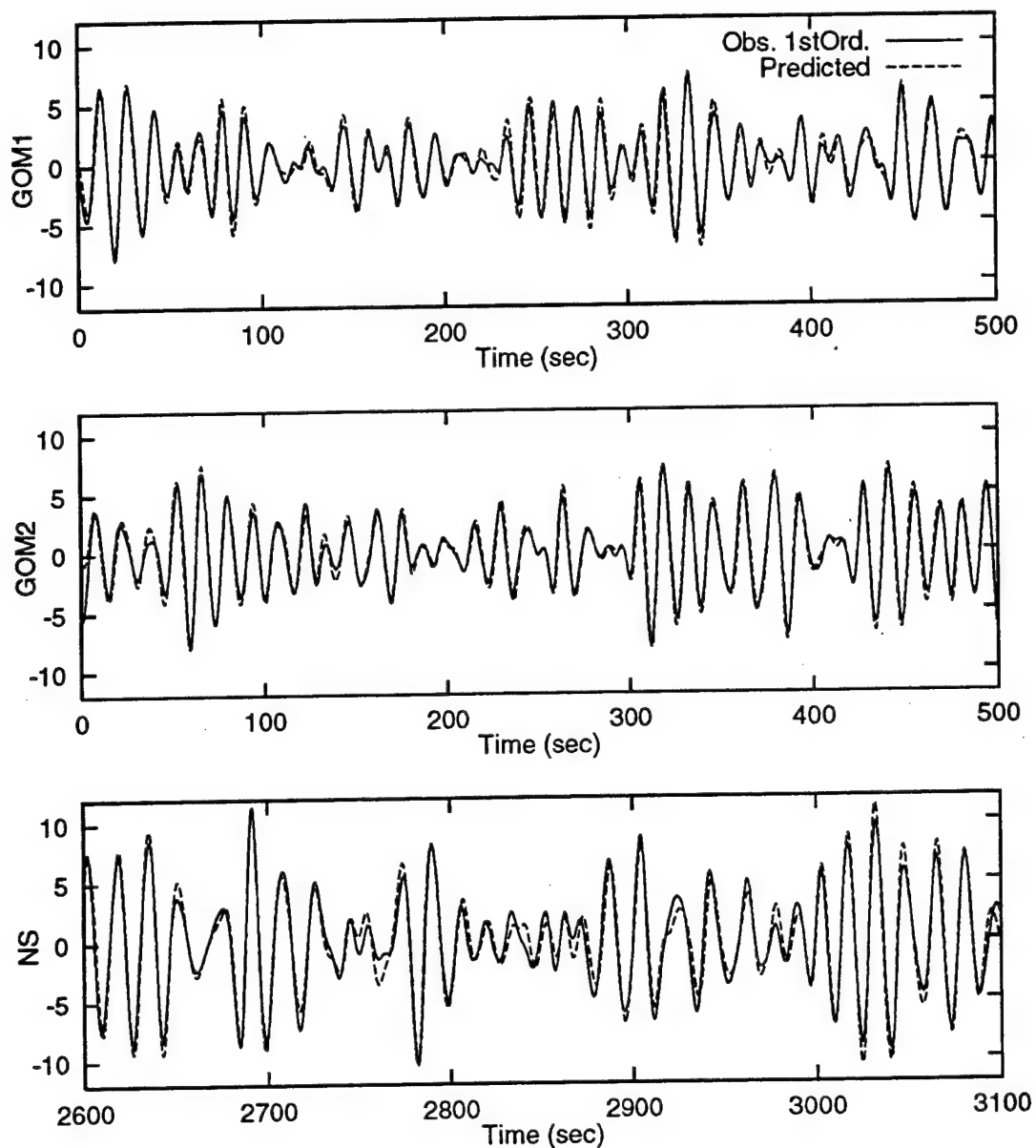


Figure 5: Predicted vs. observed first-order response histories for the three tests. For clarity we show only 500-second portions of each test, selected to include the absolute maximum observed response.

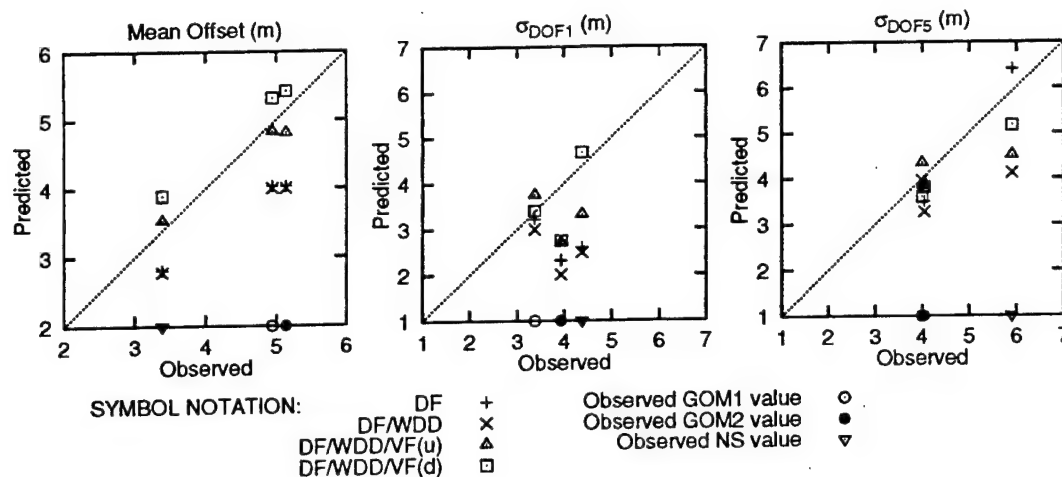


Figure 6: Predicted response mean and standard deviations vs measured results in the three tests. Standard deviations are shown for both surge and pitch frequency components.

In each case the predicted values from all 4 models are plotted against the observed value from that test. Because there are 3 tests, this results in $4 \times 3 = 12$ data points per plot. A 45-degree line implying perfect agreement is also shown.

Focusing first on the diffraction-only (DF) model, we find it underpredicts both the mean and rms in all but one of the 9 observed values. (We return below to the anomalous case, which involves the pitch rms σ_5 in the NS test.) Adding wave drift damping (DF/WDD) will not change the mean, and only weakly affects the rms predictions (again excluding the NS pitch case). This suggests the need for viscous forces, which contribute both an extra mean force (due to the asymmetric effect of wave stretching) and a slowly-varying drift force. As Figure 6 shows, the VF(u) and VF(d) models—which include viscous forces—generally give better predictions of both the mean and rms levels. Results with the disturbed wave (VF(d)) generally give slightly higher responses—both in mean and rms—than those using the undisturbed wave (VF(u)). Neither the VF(u) nor VF(d) model seems systematically closer to the observations; however, both appear superior to models that exclude viscous forces altogether.

Returning to the anomalous pitch response in the NS test, note from Table 1 that our damping calibration effectively fails in this case. Although each of the 4 models was assigned only minimal pitch damping ($\zeta_5 = .001$), all of these predict wider spectral bandwidths than that observed in the NS test. Thus the predictive models here are not “damping-tuned” to the tests as in the other cases—and the pattern of the 4 model predictions for σ_5 in the NS case is somewhat arbitrary. As to why the bandwidth mismatch may occur, recall the increased effect of limited data in the NS case: here the bandwidth estimation uses only the 1 hour test, as opposed to the 2 pooled hours used to form the predictive model for both GOM seastates.

Total Response Histories

Finally, we compare the observed and predicted 1-hour histories of the total spar displacement. Figures 7–9 show these histories for the 3 1-hour tests. All figures show the observed displacement history at the top, while 3 of the 4 corresponding predictions are shown beneath (the DF/WDD

model is omitted for clarity). Recall that our particular interest lies in predicting not only overall response statistics, but also the response evolution and potential mode-swapping (e.g., Figure 4 for the GOM1 case). Figure 7 repeats that case, and it is notable that all 3 predicted responses show a similar trend, toward greater surge response, in the second half of the GOM1 test. Note also that for extreme response events (e.g., observed response above 20m), all of the predictions show fairly good agreement. The greatest deviations, between the test and predictions, seem to occur over periods of relatively low response amplitude (e.g., times $t=0-1000s$, $1500-2300s$).

Figure 8 shows similar tendencies for the GOM2 test. Again there is good qualitative agreement: both the tests and the predictions show a period of relatively little surge (at around $t=700-2000s$), followed by a marked surge increase through the rest of the hour. Large observed responses tend to coincide with high predicted values. The magnitude of these large responses is not as well predicted, however; predictions generally underestimate the response in the critical high-surge portion ($t=2300-3600s$). In contrast, the same predictions often overestimate response in the earlier, low-surge segment ($t=700-2000s$). (This potential for mode swapping and compensating errors suggests the need here to compare observations and predictions through time history behavior, not merely through summary statistics in the time or frequency domain.)

Finally, Figure 9 shows NS test results. Again there is a transition, near the end of the test, which produces the largest amplitude responses (indeed, the largest offsets among the 3 tests). It is caused here, however, by an increase in the pitch as well as the surge component. Note that despite the potential damping mismatch in this case, the models follow this critical portion of high-amplitude pitch fairly well (from about $t=2700s$ on). As in the GOM1 case, greater deviations between models and observations occur at earlier portions of the history, involving lower amplitude responses.

COMPARING RESPONSES TO SIMULATED AND OBSERVED WAVES

The foregoing results show how well various models can predict the spar response in the OTRC tests, based on the corresponding observed wave input. Finally, we study briefly an associated question: are the observed response properties, such as mode swapping, also consistent with the response of the spar to idealized, Gaussian simulations of (first-order) random waves? If not, these observed properties may perhaps reflect special aspects of the wave input in the wave tank; e.g., the effect of its finite dimensions.

As earlier noted, both surge and pitch rms components of the observed spar motions vary notably over periods of roughly 20-30 minutes. We quantify this rms variation by (1) splitting the response into 20-minute segments; (2) calculating the rms values, $\sigma_1 \dots \sigma_n$, in each of the n segments; and (3) forming the sample mean $\bar{\sigma} = \sum_i \sigma_i / n$ and variance $s_\sigma^2 = \sum_i (\sigma_i - \bar{\sigma})^2 / (n - 1)$. We focus here on the two GOM tests, yielding 2 hours and hence $n=6$ 20-minute segments with associated rms values $\sigma_1 \dots \sigma_6$. The resulting s_σ values are found to be

$$s_\sigma = 1.22m \text{ (surge)}; \quad s_\sigma = 0.50m \text{ (pitch)} \quad (3)$$

For comparison we simulate† multiple 2-hour spar histories, and process each as we did the 2-hour test to find a corresponding s_σ estimate. These s_σ estimates from our simulations yield the following

†These simulations use the DF/WDD/VF(u) model, and first-order Gaussian waves are simulated from a JON-SWAP spectrum with $H_s=14m$, $T_p=14s$, and $\gamma=2$. The diffraction analysis internally applies second-order corrections to the (assumed) first-order wave input; hence the Gaussian model is consistent here. Drag forces for this model use the total undisturbed wave; for simplicity we use the Gaussian waves here as well. Alternatively, one may add second-order wave contributions to better approximate the total undisturbed wave.

mean $E[s_\sigma]$ and standard deviation $D[s_\sigma]$:

$$E[s_\sigma] = 1.26\text{m (surge)}; \quad E[s_\sigma] = 0.95\text{m (pitch)} \quad (4)$$

$$D[s_\sigma] = 0.47\text{m (surge)}; \quad D[s_\sigma] = 0.45\text{m (pitch)} \quad (5)$$

Thus, while the observed modal rms values may seem highly variable, our simulations show similar or *still greater* variability (especially in pitch). Note also that the $D(\cdot)$ values here reflect variability in s_σ estimates from different $T=2$ hour segments. (If T increases, $D(\cdot)$ should decay like $T^{-1/2}$.) Because Eq. 3 uses 1 $T=2$ hour segment, these $D(\cdot)$ values suggest the following mean ± 1 -sigma intervals on the test estimates: $s_\sigma=1.22 \pm 0.47$ in surge and $s_\sigma=0.50 \pm 0.45$ in pitch. As even these relatively narrow, 1-sigma confidence intervals include the average simulation results (Eq. 4), it is difficult to find statistically significant differences between the tests and the simulations.

CONCLUSIONS

Four models have been established to predict the along-wave motions of a spar buoy in random seas. These have been implemented and compared with wave tank measurements of the spar displacement, at a reference elevation $z=54.8\text{m}$ above the mean water level. Results are shown across 3 1-hour tests of 100-year extreme wave conditions. Specific methods and results include the following:

- In all of the tests, the main rms contribution comes from the resonant response in surge and pitch modes, at periods of roughly 330s and 70s respectively (e.g., Figure 3). This shows the need for models of nonlinear forces—diffraction, drag or both—to explain not only the mean offset but also the amplitude of slow-drift oscillations of the spar.
- The significant low-frequency resonant response also implies the need for accurate estimates of damping, in both the surge and pitch modes of the spar. We show how these modal dampings can be estimated from response spectral moments. The resulting dampings are “consistent” with the other features of the model; for example, the explicit addition of wave drift damping (WDD) is accompanied by lower levels of the remaining damping in the model (Table 1).
- The wave-frequency response has been found to be fairly well predicted across all 3 tests (Figure 5). This reflects the modelling adequacy of linear diffraction forces and the spar’s mass properties. Regarding slow-drift response, models that include only diffraction forces generally underestimate both the mean and rms response levels (Figure 6). To address this, we introduce additional models that include viscous forces, based on either the undisturbed (far-field) wave or the actual disturbed wave in the presence of the spar. While it is difficult to conclude which of these is generally more accurate, both appear superior to models that exclude viscous forces altogether.
- The observed responses display considerable “mode-swapping” between surge and pitch modes (e.g., Figure 4). Figures 7–9 show that our predictive models, which use the observed wave and its underlying first-order components, can produce qualitatively similar behavior. They generally follow the observed trend, in all three tests, toward larger amplitude responses near the end of the hour. This trend manifests itself in the Gulf of Mexico tests by a late increase in surge-induced response (Figures 7–8), and in the North Sea test by enhanced pitch response as well (Figure 9).
- While the modal rms values in the tests appear rather variable, long simulations with Gaussian (first-order) waves show similar or *still greater* variability (Eqs. 3–5). From the limited 2-hour duration of GOM tests, it is difficult to find statistically significant differences between these tests and the simulations.

Acknowledgements

Support for this work has been provided by the National Science Foundation, through a grant from its Offshore Technology Research Center. We gratefully acknowledge the OTRC for their ongoing technical and financial support.

REFERENCES

- Glanville, R.S., J.R. Pauling, J.E. Halkyard, and T.J. Lehtinen (1991). Analysis of the spar floating drilling production and storage. *Proc., Offshore Tech. Conf.*, Houston, Paper OTC-6701, 57-68.
- Jha, A.K. (1997). *Nonlinear stochastic models for ocean wave loads and responses of offshore structures and vessels*, Ph.D. thesis, Civil Eng. Dept., Stanford University.
- Kim, M.H. and D.K.P. Yue (1989). The complete second-order diffraction solution for an axisymmetric body. Part 1: Monochromatic incident waves. *Journal of Fluid Mech.*, **200**, 235-264.
- Kim, M.H. and D.K.P. Yue (1991). Sum- and difference-frequency wave loads on a body in unidirectional Gaussian seas. *J. Ship Res.*, **35**, 127-140.
- OTRC, Vol. I. (1995). *Spar model test: joint industry project*, Final Report, Offshore Technology Research Center.
- Ran, Z., M.H. Kim, J.M. Niedzwecki, and R.P. Johnson (1996). Responses of a spar platform in random waves and currents (experiment vs. theory). *Int. Journal of Offshore and Polar Eng.*, **6**(1), 27-34.
- Ude, T.C. (1994). *Second-order load and response models for floating structures: probabilistic analysis and system identification*, Ph.D. thesis, Civil Eng. Dept., Stanford University.
- Ude, T.C. and S.R. Winterstein (1996). Calibration of slow-drift motions using statistical moments of observed data. *Proc., 6th Int. Conf. Offshore & Polar Eng.*, Los Angeles.
- Vanmarcke, E. (1972). Properties of spectral moments with applications to random vibration. *J. Engrg. Mech.*, ASCE, **98**, .
- Weggel, D.C. and J.M. Roesset (1996). Second-order dynamic response of a large spar platform: numerical predictions versus experimental results. *Proc., 15th Int. Conf. Offshore Mech. & Arctic Eng.*, Florence.
- Wheeler, J.D. (1970). Method for calculating forces produced by irregular waves. *Journal of Petroleum Tech.*, 359-367.
- Winterstein, S.R. and A.K. Jha (1997). Random nonlinear ocean waves: a method to identify first- and second-order effects. *J. Engrg. Mech.*, ASCE, Submitted for possible publication.

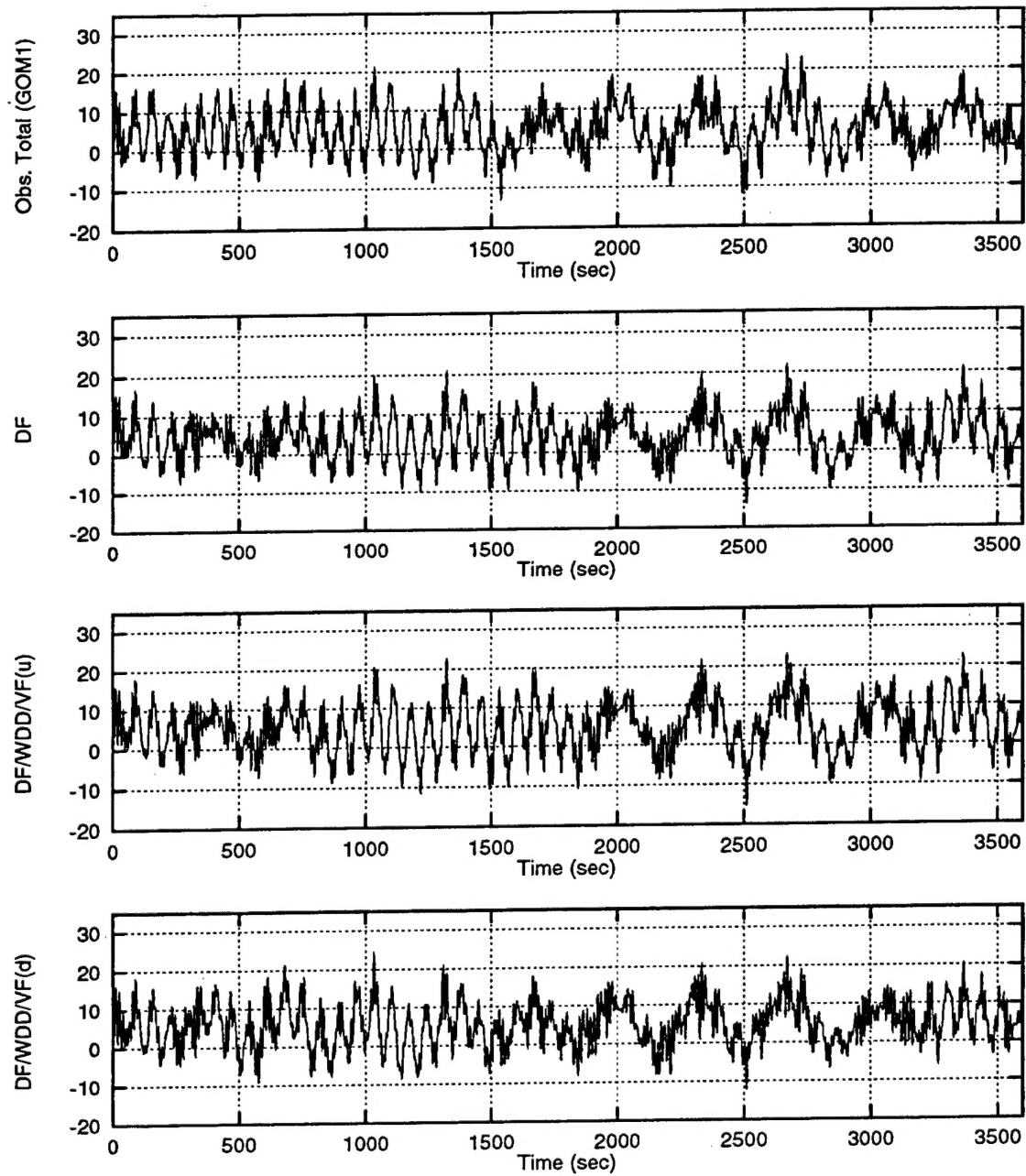


Figure 7: Combined (total) surge response time history for GOM1: prediction vs. measurement.

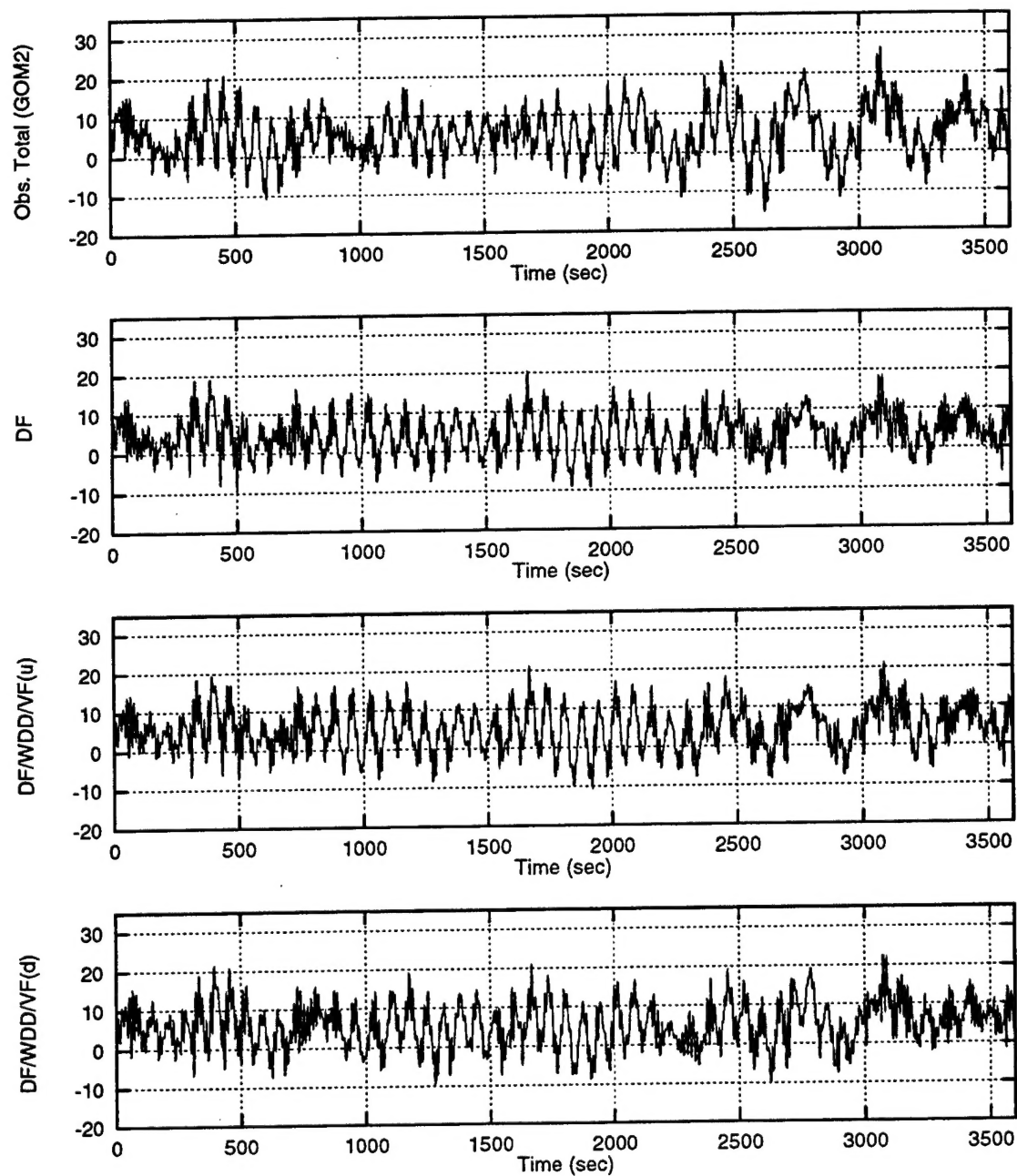


Figure 8: Combined (total) surge response time history for GOM2: prediction vs. measurement.

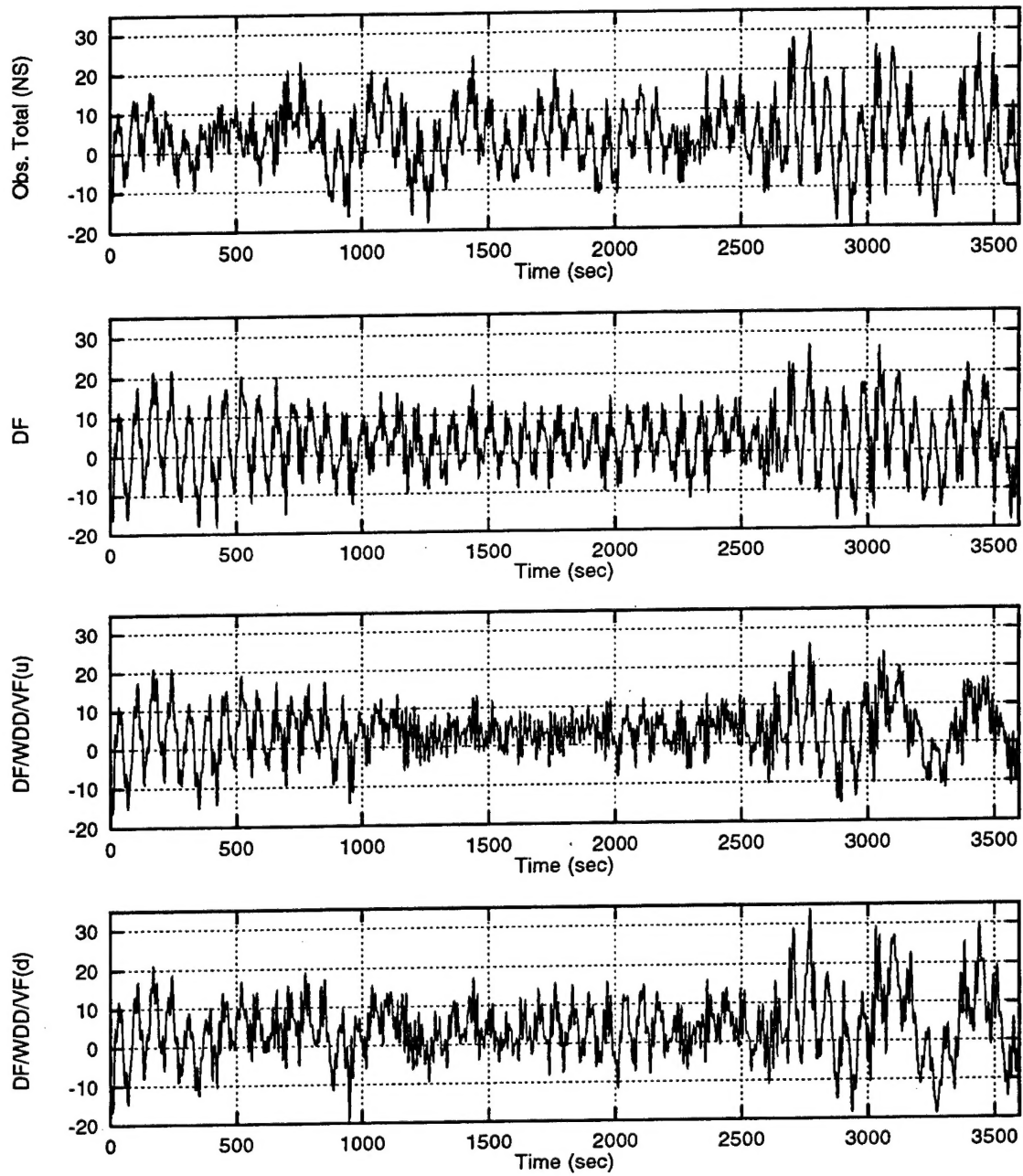


Figure 9: Combined (total) surge response time history for NS: prediction vs. measurement.

REPORT DOCUMENTATION PAGE

Form Approved
OMB No. 0704-0188

Public reporting burden for this collection of information is estimated to average 1 hour per response, including the time for reviewing instructions, searching data sources, gathering and maintaining the data needed, and completing and reviewing the collection of information. Send comments regarding this burden estimate or any other aspect of this collection of information, including suggestions for reducing this burden to Washington Headquarters Service, Directorate for Information Operations and Reports, 1215 Jefferson Davis Highway, Suite 1204, Arlington, VA 22202-4302, and to the Office of Management and Budget, Paperwork Reduction Project (0704-0188) Washington, DC 20503.

PLEASE DO NOT RETURN YOUR FORM TO THE ABOVE ADDRESS.

1. REPORT DATE (DD-MM-YYYY) 00-06-1997		2. REPORT DATE June, 1997		3. DATES COVERED (From - To)	
4. TITLE AND SUBTITLE Spar Floating Platform: Numerical Analysis and Comparison with Data.				5a. CONTRACT NUMBER	
				5b. GRANT NUMBER N00014-96-1-0641	
				5c. PROGRAM ELEMENT NUMBER	
6. AUTHOR(S) Alok K. Jha				5d. PROJECT NUMBER	
				5e. TASK NUMBER	
				5f. WORK UNIT NUMBER	
7. PERFORMING ORGANIZATION NAME(S) AND ADDRESS(ES) RMS Group S.R. Winterstein, C.A. Cornell Blume Center Stanford University, CA 94305				8. PERFORMING ORGANIZATION REPORT NUMBER RMS-25	
9. SPONSORING/MONITORING AGENCY NAME(S) AND ADDRESS(ES) OFFICE OF NAVAL RESEARCH 800 N. QUINCY ST. ARLINGTON, VA 22217-4620 ATTN: ROSEHDY BARSOLINI				10. SPONSOR/MONITOR'S ACRONYM(S)	
				11. SPONSORING/MONITORING AGENCY REPORT NUMBER	
12. DISTRIBUTION AVAILABILITY STATEMENT APPROVED FOR PUBLIC RELEASE					
13. SUPPLEMENTARY NOTES					
14. ABSTRACT Second-Order nonlinear models are applied to study the global response of a Spar floating platform. Physical model test results are compared with those resulting from a numerical model of the spar as a rigid body with six degrees of freedom. The incident wave loads are modeled as a second-order phenomenon. The response quantity of interest is the total horizontal displacement near the spar deck. The numerical model is found to yield reasonable predictions when compared to the measured results in the model tank.					
15. SUBJECT TERMS					
16. SECURITY CLASSIFICATION OF:			17. LIMITATION OF ABSTRACT	18. NUMBER OF PAGES	19a. NAME OF RESPONSIBLE PERSON
a. REPORT	b. ABSTRACT	c. THIS PAGE			19b. TELEPHONE NUMBER (Include area code)